The Astrophysical Journal, 699:186–214, 2009 July 1 doi:10.1088/0004-637X/699/1/186

DYNAMICS OF IONIZED GAS AT THE GALACTIC CENTER: VERY LARGE ARRAY OBSERVATIONS OF THE THREE-DIMENSIONAL VELOCITY FIELD AND LOCATION OF THE IONIZED STREAMS IN SAGITTARIUS A WEST

Jun-Hui Zhao[1], Mark R. Morris[2], W. M. Goss[3], and Tao An[4]
[1] Harvard-Smithsonian CfA, 60 Garden St, Cambridge, MA 02138, USA; jzhao@cfa.harvard.edu
[2] Department of Physics and Astronomy, UCLA, 405 Hilgard Avenue, Los Angeles, CA 90095, USA
[3] NRAO, P.O. Box O, Socorro, NM 87801, USA
[4] Shanghai Astronomical Observatory, Chinese Academy of Sciences, Shanghai 200030, China
Received 2009 January 12; accepted 2009 April 22; published 2009 June 10

ABSTRACT

We present new results based on high-resolution observations of Sgr A West at the Galactic center with the Very Large Array (VLA) at 1.3 cm. By combining recent observations with those made at earlier epochs with the VLA at wavelengths of 1.3 and 3.6 cm, we measured proper motions for 71 compact H II components in the central 80″ (3 pc, assuming $D = 8$ pc). Using VLA archival data for the H92α radio recombination line, we also investigated radial velocities in the LSR velocity range from +200 to –415 km s^{-1}. Combining proper motion and radial velocity measurements, we have determined the three-dimensional velocity distribution in Sgr A West. We find that the three ionized streams (Northern Arm, Eastern Arm, and Western Arc) in the central 3 pc can be modeled with three bundles of Keplerian orbits around Sgr A*. Assuming that each of the observed streams of ionized gas follows a single orbit, we determined the five orbital parameters (a, e, Ω, ω, i) for each of them using least-square fitting to the loci of the streams. The degeneracy in the orbital solutions for both the direction of flow and the two mirror images can be further resolved using the information obtained from the velocity measurements. Our results confirm earlier results on the streams in the Western Arc and the Northern Arm to be in Keplerian orbits, suggesting that the stream in the Eastern Arm is also consistent with an elliptical orbit. All three are confined within the central 3 pc. Both the Northern and Eastern Arm streams have high eccentricities ($e = 0.83 \pm 0.10$ and 0.82 ± 0.05, respectively), while the Western Arc stream is nearly circular, with $e = 0.2 \pm 0.15$. All three streams orbit around Sgr A* in a counterclockwise sense (viewed from the Earth) and have orbital periods in the range $4–8 \times 10^4$ yr. To verify the fit, the distributions of radial and transverse velocity vectors in Sgr A West were also computed using the Keplerian model and they show good agreement with both the proper motion and radial velocity data. In addition, the computed orbits suggest that the Northern and Eastern Arm streams may collide in the "Bar" region (a few arcsec south of Sgr A*) and that most of the orbiting ionized gas in the "Bar" region is located behind Sgr A*. We also report an ionized nebula associated with IRS 8, including a bow shock in radio continuum emission which shows excellent agreement with near infrared observations. From the H92α line data, we find evidence of substantial interaction between the IRS 8 nebula and the Northern Arm stream occurring in the bow-shock region. Other new morphological features revealed in our high-resolution image include (1) a helical structure in the Northern Arm, suggesting that MHD plays an important role in the motion of the ionized gas, in addition to the dynamics determined by the central gravitational field, and (2) a linear feature in the IRS 16 region, suggesting that the compressed edge of the Northern Arm may result from the collective winds and radiation pressure from the high mass stars in the IRS16 cluster.

Key words: Galaxy: center – H II regions – ISM: individual (Sagittarius A West) – ISM: kinematics and dynamics – radio lines: ISM

1. INTRODUCTION

Proper motion measurements of infrared (IR) stars in the central 1″ of the Galaxy suggest the existence of a supermassive black hole (SMBH) with a mass of several million solar masses ($M_\odot$) at the position of the compact radio source Sgr A* (Schödel et al. 2002; Ghez et al. 2003, 2005). A recent determination of the mass ($4.2 \times 10^6\ M_\odot$) has been reported by Ghez et al. (2008) and Gillessen et al. (2009). The radio source size, 37^{+16}_{-10} μas, was determined with recent very long baseline interferometry (VLBI) observations at 1.3 mm, suggesting that the intrinsic shape of Sgr A* is not symmetric about the SMBH and that it arises from the surrounding accretion flow (Doeleman et al. 2008). Accretion onto Sgr A* must also be fed at various times by the numerous gas streams that have been observed in the surrounding H II region, Sgr A West, notably the ionized "mini-spiral" arms discovered by Lo & Claussen (1983) and Ekers et al. (1983) with the Very Large Array (VLA). The VLA and IR observations have revealed that Sgr A West consists of high velocity bulk flows toward, or around, Sgr A*. The radial velocity fields of the ionized flows were imaged based on IR observations of the [Ne II] 12.8 μm fine-structure line (Lacy et al. 1980; Serabyn & Lacy 1985; Serabyn et al. 1988), the IR recombination lines Br-α and/or Br-γ,(Geballe et al. 1987; Herbst et al. 1993; Paumard et al. 2004) and VLA observations of the H76α line (Schwarz et al. 1989) and the H92α line (Roberts & Goss 1993; Roberts et al. 1996). Schwarz et al. (1989) found a nearly complete ionized ring from the H76α line data and the kinematics of this ionized ring could be modeled with a circular orbit. Lacy et al. (1991) interpreted the kinematics combining the Northern Arm and Western Arc as a one-armed spiral in a Keplerian disk with nearly circular orbits. Later, Roberts & Goss (1993) used VLA observations of the H92α line to divide the ionized "ring" into three separate components: the Western Arc, which is indeed in circular motion, the Northern Arm, and the Bar. The H92α line

observations were subsequently used by Liszt (2003) to argue that the Bar and Eastern Arm together represent a single stream of gas orbiting about the Galactic center. Recently, Paumard et al. (2004) used observations of the Br-γ line to suggest that the motions of the ionized stream in the Northern Arm could be fitted with a family of elliptical, Keplerian orbits.

Using high-resolution radio observations, the motions of the H II components on the sky plane can be elucidated. Large proper motions of the H II components were inferred from data acquired during the period 1991–1997 (Yusef-Zadeh et al. 1998; Zhao & Goss 1998, 1999). A noticeable fraction of the H II components shows large motions that cannot be explained purely in terms of the bounded orbital motions occurring in reaction to the central gravitational field. The large peculiar motions might be explained by stellar winds or stellar wind interactions, possible explosive events, or debris ejected from a partially disrupted stellar envelope of a star due to the tidal force near the SMBH. These explanations need to be assessed with the improved observations presented here.

In this paper, we present new results on the dynamics of the ionized gas in the central 3 pc of the Galaxy based on VLA measurements of three-dimensional velocities, along with numerical modeling. Section 2 describes observations and data reductions. Section 3 shows the measurements of proper motions and radial velocities. Section 4 presents the results on the three-dimensional velocities of individual sources and regions. Section 5 describes the dynamical models for the mini-spiral arms in Sgr A West. Section 6 discusses an MHD effect on the detailed structure of the ionized streams. Section 7 summarizes the results and conclusions.

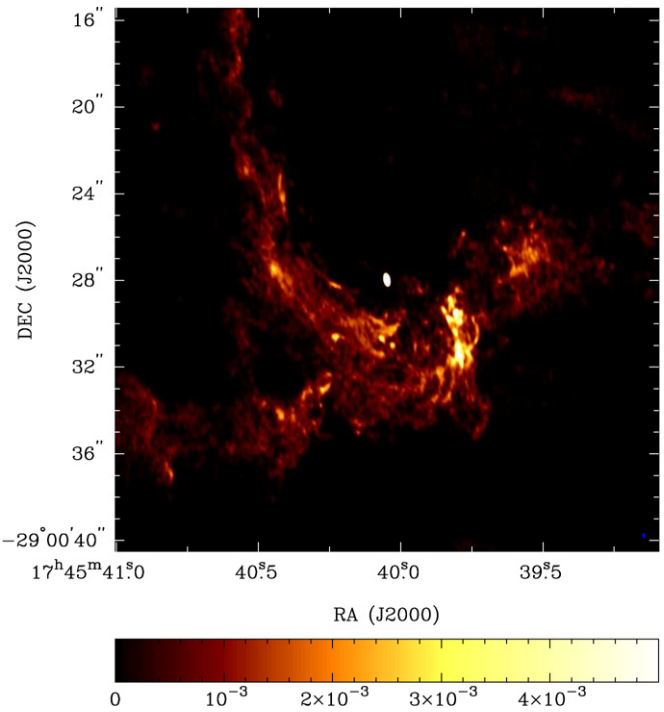

Figure 1. VLA continuum image of the central 25″ (833 × 833 pixels) of Sgr A West at 1.3 cm, made with the epoch 2005K data with FWHM = 0.″2 × 0.″1 (P.A. = 11°; right bottom). The size of the original image is 8192 × 8192 pixels, constructed with all the visibility data (not filtered) sampled with the VLA in A and B configurations. The color wedge (bottom) shows the intensity of the continuum in units of Jy beam^{-1}. The rms noise is 20 μJy.

2. OBSERVATIONS AND DATA REDUCTIONS

2.1. Data at 1.3 cm

The new observations of Sgr A* and its vicinity were made at 1.3 cm on 2004 December 23 and 2005 April 26 with the VLA in its A and B configurations, respectively, in order to better determine the proper motions of the H II components near Sgr A* with a long time span. Table 1 summarizes the observations and data that are used in this paper. At 1.3 cm, all the observations were made in the continuum mode with a total bandwidth of 100 MHz. The flux density scales for each of the data sets were determined using the primary calibrators 3C 286 and 3C 48 following the standard VLA calibration procedure in the Astronomical Image Processing System (AIPS). The complex gains were calibrated using the quasi-stellar object (QSO) NRAO 530. In order to remove the time variability of Sgr A*, the flux density of the point source was measured in time bins of 0.5 hr. Then the time variation in flux density from Sgr A* was accounted for using the technique described in Zhao et al. (1991) so that these variations do not lead to uncorrected sidelobe emission that could affect the proper motion determinations. In addition, archive data taken by different groups using different pointing positions slightly offset from Sgr A* are in B1950 or J2000 coordinate systems. We therefore recalculated the coordinates in each of the data sets with UVFIX in AIPS, converting all coordinate frames to the J2000 equinox and shifting the phase centers to the position of Sgr A*. The errors owing to differential aberration caused by the on-line program were automatically corrected with the off-line program UVFIX. Further corrections for the baseline-based residual errors were applied using the gains determined from the model of NRAO 530. Then, the data from the observations in the consecutive A and B configurations were combined to form separate epoch data sets for the proper motion measurements. The remaining residual errors in the complex gains of each data set were further corrected in both phase and amplitude using the self-calibration technique. Weighting by the number of visibilities in each combined data set, we determined effective dates of the three combined data sets to be MJD 53419 (2005 February 18), MJD 51422 (1999 September 1), and MJD 48485 (1991 August 17), spanning 13.5 years. Hereafter, we refer to these epochs' data sets as 2005K, 1999K, and 1991K, respectively.

A dirty image at 1.3 cm was constructed by applying an FFT of the 2005K data with robustness weighting of $R = 0$. The dirty image was cleaned with the Clark–Steer hybrid algorithm and the clean component image was convolved with a Gaussian beam and the resultant FWHM beam is 0.″2 × 0.″1 (P.A. = 11°). The rms noise of the "cleaned" image (Figure 1) is 20 μJy and the peak flux density is >1 Jy beam^{-1}. The dynamical range of the image is >50,000:1. With higher system temperatures at the earlier epochs, the images of 1999K and 1991K have higher rms fluctuations of 40 and 50 μJy, respectively. The delay beam in the image at 1.3 cm is 92″ × 46″(P.A. = 11°) and the source offsets from the delay center are all less than 16″ in the measurements. Thus, the effects due to the delay beam can be neglected.

2.2. Data at 3.6 cm

At 3.6 cm, a total of nine observations was acquired from the VLA archive. All the observations were made in the spectral line mode for the H92α line. The flux density scale was determined using 3C 286 and 3C 48. The calibration for complex gains utilized NRAO 530 following the AIPS procedure. In addition, we also corrected for the bandpass shape using 3C 84 and

Table 1
Log of Data and Observations

Date (YYYY MM DD)	R.A. (B1950)	Decl. (B1950)	ν (GHz)	ν_0 (GHz)	$V_{\rm lsr}$ (km s^{-1})	$\Delta\nu$ (MHz)	N-chan	Array Config.
Continuum Observations at 1.3 cm								
2005 Apr 26	17:42:29.3180	−28:59:18.390	22.485	...	...	50	2	B
2004 Dec 23	17:42:29.3180	−28:59:18.390	22.485	...	...	50	2	A
1999 Nov 16	17:42:29.3180	−28 59 18.390	22.485	...	...	50	2	B
1999 Aug 19	17:42:29.3180	−28 59 18.390	22.485	...	...	50	2	A
1992 Jan 19	17:42:29.3180	−28 59 18.390	22.235	...	...	50	2	B
1991 Jun 22	17:45:40.0848[a]	−29:00:27.779[a]	22.235	...	...	50	2	A
H92α Line Observations at 3.5 cm								
2002 May 22	17:42:29.3000	−28:59:17.000	8.3156	8.3094	−200	0.3906	31	BnA
2002 May 21	17:42:29.3000	−28:59:17.000	8.3156	8.3094	−200	0.3906	31	BnA
1999 Oct 18	17:42:29.3000	−28:59:17.000	8.3145	8.3094	−200	0.3906	31	BnA
1999 Oct 17	17:42:29.3000	−28:59:17.000	8.3145	8.3094	−200	0.3906	31	BnA
1993 Feb 13	17:42:29.3000	−28:59:17.000	8.3159	8.3094	−200	0.3906	31	BnA
1993 Feb 12	17:42:29.3000	−28:59:17.000	8.3159	8.3094	−200	0.3906	31	BnA
1991 Feb 19	17:42:29.3000	−28:59:17.000	8.3104	8.3094	0	0.3906	31	D
1990 Oct 2	17:42:29.3000	−28:59:17.000	8.3089	8.3094	0	0.3906	31	CnB
1990 Jul 2	17:42:29.3000	−28:59:17.000	8.3095	8.3094	0	0.3906	31	BnA

Note. [a] The J2000 equinox was used for the observations.

NRAO 530. We corrected flux density variations of Sgr A* using the method discussed by Zhao et al. (1991).

The on-line effect of differential aberration was corrected with the same procedure as used for the data at 1.3 cm. The phase centers of all the data sets were shifted to the same common position for Sgr A*. We combined two data sets taken in the BnA configuration on 2 consecutive days to form four epochs' data sets (2002X, 1999X, 1993X, and 1990X). The effective dates of the four data sets—MJD 52415.5 (2002 May 22), MJD 51468.5 (1999 October 18), MJD 49030.5 (1993 February 13), and MJD 48075.5 (1990 July 4)—span nearly 12 years.

Combining all the data at 3.6 cm, we constructed a 8192 × 8192 dirty image with robustness weighting $R = 0$ and the multifrequency synthesis technique, which avoids the bandwidth smearing effect. Thus, the frequency dependence of the *uv* coordinate was used to provide better *uv* coverage and to minimize frequency smearing. The cleaned image shown in Figure 2 was achieved with the Clark–Steer hybrid deconvolution algorithm, convolving with the synthesized beam FWHM = 0.″70 × 0.″57 (57°). The rms noise is 20 μJy and the peak flux density is 0.8 Jy beam^{-1}, giving a dynamical range of 40,000:1.

3. MEASUREMENTS OF THREE-DIMENSIONAL VELOCITIES

3.1. Proper Motion

Both the *K*-band and *X*-band data sets were used for proper motion measurements. In order to eliminate confusion from the extended, diffusion emission in Sgr A West, we filtered out the short baseline data in the imaging process. We constructed images at each epoch with the visibility data at projected baseline lengths $> 100k\lambda$ at both 1.3 and 3.6 cm. The cleaned images were convolved to the common synthesized beams of 0.″2 × 0.″1 (P.A. = 0°) and 0.″6 × 0.″5 (P.A. = 0°) at 1.3 and 3.6 cm, respectively. Then, we fitted each of the compact H II components with a single Gaussian and a slope that removes the continuum baseline. The peak position offsets $\Delta\alpha, \Delta\delta$ from Sgr A* were determined in the J2000 coordinate system along with 1σ errors in the least-square (LSQ) fitting. All source positions were determined as offsets from Sgr A*. The motions of the H II components with respect to Sgr A* can be determined from the difference in the position offsets between two epochs. In order to minimize the systematic errors, we made the best fit to all the measurements $(\Delta\alpha_i, \Delta\delta_i)$ at each epoch (t_i) using a linear regression. The slopes μ_α and μ_δ corresponding to proper motions in right ascension and declination, along with the position offsets $(\Delta\alpha_0, \Delta\delta_0)$ at reference time t_0, can be determined from the linear fitting. Figure 3 shows the linear fitting to the position offsets and the determination of the proper motions. Table 2 summarizes the measurements of the proper motions. Columns 3 and 4 in Table 2 list the peak position offsets at epochs 2005K and 2002X for 1.3 and 3.6 cm, respectively. The deconvolved sizes of the major ($\theta_{\rm maj}$) and minor ($\theta_{\rm min}$) axes and the position angle (P.A.) of the sources, along with their 1σ errors are given in Column 5. The measurements of the proper motions (μ_α, μ_δ) are given in Columns 6 and 7. The proper motion vectors determined from both the 1.3 and 3.6 cm data are overlaid on the continuum image of Sgr A West at 3.6 cm (Figure 2).

3.2. Radial Velocity

3.2.1. Construction of the H92α Line Cube

The H92α line ($\nu_0 = 8309.393$ MHz) observations were centered at two radial velocities (see Table 1), 0 km s^{-1} at the early epochs (before 1992) and −200 km s^{-1} at the epochs after 1993. The observations can be calibrated to form two line cubes at 0 km s^{-1} and −200 km s^{-1}, respectively. Both data cubes have 31 channels, with a channel width of 0.3906 MHz, corresponding to 14.1 km s^{-1} in velocity resolution. Excluding the first channel due to poor bandpass signals in the correlator configuration, each of the cubes covers a velocity range of 423 km s^{-1}. Due to the broad velocity distribution of the H92α line in the range from –350 to +350 km s^{-1} in the Galactic center region, none of the observations covers the full extent of the line emission. This limitation makes it difficult to construct a continuum-free line cube. The final line cubes were made using the following technique: (1) for the −200 km s^{-1} data cube, we used channels 29 and 30 at velocities of −383 and −397

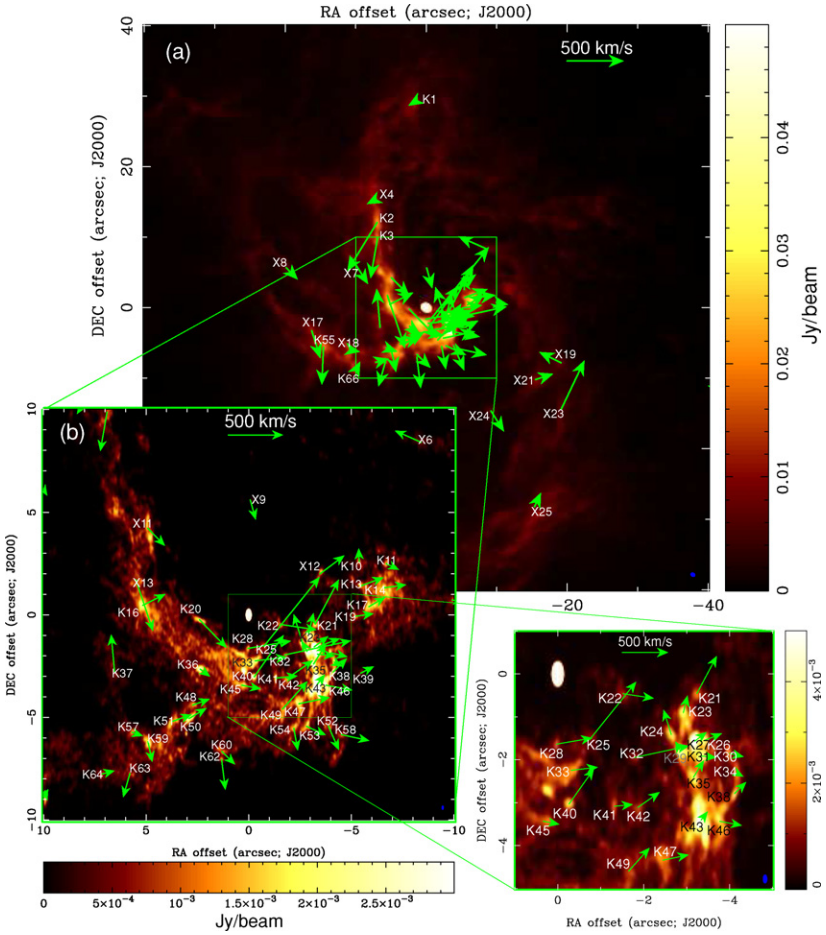

Figure 2. (a) The VLA continuum image of Sgr A West at 3.6 cm (background) made by combining all the data listed in Table 1, with all the baselines that are not filtered. The FWHM of the beam (right-bottom corner) is $0\farcs70 \times 0\farcs57$ (P.A. $= 57°$). The color wedge to the right shows the intensity of the continuum emission in units of Jy beam^{-1}. Proper motion vectors of the 71 H II knots (Table 2) in Sgr A West are overlaid on the radio continuum image. (b) The inset (foreground) shows the proper motion vectors in the inner $20'' \times 20''$region, overlaid on the continuum image at 1.3 cm (Figure 1). (c) The inset at left-bottom shows the inner $6'' \times 6''$ region. The velocity scaling vectors for proper motions are shown in each of the images.

km s^{-1} to represent the line-free channels and concatenate them to the other end of the -200 km s^{-1} cube; (2) using UVLIN, the continuum emission was linearly interpolated and the fitted continuum emission was subtracted from the *uv* data across the line cube to produce continuum-free line data. For the 0 km s^{-1} cube, there are essentially no line-free channels. However, the two line cubes overlap in the velocity range 0 to -200 km s^{-1}. We averaged the four overlapping channels at velocities ranging from -169 to -212 km s^{-1}. In the same velocity range, the line emission can be determined from the -200 km s^{-1} cube. A line-free channel was created by subtracting the line emission from the averaged channel. Then, the line-free channel was attached to both ends of the 0 km s^{-1} cube and the continuum level was interpolated linearly across the line cube. Again the fitted continuum was subtracted from the visibility data to form the line (continuum-free) cube. We note that this technique works only if the change (ΔS) of the continuum flux density (S) over the velocity range ($\Delta V = 550$ km s^{-1} or $\Delta\nu = 15.3$ MHz) is less than the noise-to-signal ratio, namely $\left|\frac{\Delta S}{S}\right| \approx \left|\alpha\frac{\Delta\nu}{\nu}\right| < \frac{\sigma_{\rm ch}}{S}$, where $S \propto \nu^{-\alpha}$ and 1 $\sigma_{\rm ch}$ noise in each channel. For the optically thin free–free emission from Sgr A West, $\alpha \sim 0.1$ and $\left|\frac{\Delta S}{S}\right| \approx 0.002\alpha = 0.0002$. The uncertainties introduced from the continuum subtraction is much less than the thermal noise.

At this point, we regridded the visibility data by interpolating the velocity so that the velocities at the adjacent channels between the 0 km s^{-1} and -200 km s^{-1} cubes are matched. The final velocity separation between channels is then resampled to 15 km s^{-1}.

Furthermore, the two image line cubes were constructed from the 0 km s^{-1} and -200 km s^{-1} image line data cubes with robustness weighting (R= 0). Using the robustness parameters of 0 and 2, we achieved the synthesized beams of $1\farcs0 \times 0\farcs95$ (19°) and $1\farcs0 \times 0\farcs83$ (3°) for the 0 km s^{-1} and –200 km s^{-1} image line cubes, respectively. The two image cubes were combined to form the final high-resolution line image cube by convolving the synthesized image to a circular beam of $1\farcs25$. We also convolved the line image cube to a large circular beam ($2''$) to detect a low surface brightness structure at larger scales. The rms fluctuations over the cube were not uniform with values with 0.15 mJy beam^{-1} for the channels from the -200 km s^{-1} data cube and 0.27 mJy beam^{-1} for the 0 km s^{-1} data cube.

Figure 4 shows the channel images covering the velocity range –415 to 200 km s^{-1}. The current data are in good agreement with the data of Roberts & Goss (1993) except for the "Bar," the mini-cavity, and the IRS 6 region where the high negative-velocity range ($V_{\rm LSR} < -212$ km s^{-1}) was not covered by these authors. The high negative-velocity components were imaged separately and discussed by Roberts et al. (1996).

Table 2
Measurements of Proper Motion and Radial Velocity

Source	IR ID	$\Delta\alpha$ (J2000)[a] (arcsec)	$\Delta\delta$ (J2000)[a] (arcsec)	$\theta_{\rm maj} \times \theta_{\rm min}$ (P.A.)[b] (arcsec×arcsec (deg))	μ_α[c] (mas yr^{-1})	μ_δ[c] (mas yr^{-1})
Measurements from 1.3 cm Observations						
K1	IRS8	1.400 ± 0.002	29.328 ± 0.002	0.44 × 0.15 (142)	1.8 ± 0.4	−1.1 ± 0.5
K2		6.956 ± 0.004	11.950 ± 0.016	1.97 × 0.32 (168)	6.8 ± 1.3	−28.0 ± 5.4
K3		6.901 ± 0.003	9.873 ± 0.008	1.27 × 0.32 (168)	1.6 ± 0.6	−9.4 ± 2.1
K8	IRS10W	6.558 ± 0.008	5.034 ± 0.004	0.56 × 0.45 (164)	0.31 ± 0.67	−1.9 ± 0.8
K10	MP–5.30+2.90	−5.390 ± 0.002	2.564 ± 0.003	0.35 × 0.26 (22)	0.2 ± 0.3	3.3 ± 0.7
K11[d]		−6.704 ± 0.001	2.500 ± 0.002	0.22 × 0.08 (166)	−3.0 ± 0.3	−1.5 ± 0.6
K13[d]		−5.482 ± 0.002	1.417 ± 0.002	0.35 × 0.12 (64)	−5.4 ± 0.3	2.0 ± 0.4
K14[d]		−6.592 ± 0.003	1.319 ± 0.003	0.27 × 0.17 (70)	−5.3 ± 0.7	0.7 ± 0.8
K15		−9.915 ± 0.003	0.724 ± 0.005	0.37 × 0.21 (160)	−2.8 ± 0.5	−0.5 ± 1.0
K16	IRS1W	5.169 ± 0.002	0.460 ± 0.002	0.49 × 0.28 (39)	−5.5 ± 0.4	2.7 ± 0.5
K17[d]		−5.858 ± 0.002	0.398 ± 0.002	0.37 × 0.22 (156)	−3.9 ± 0.4	2.3 ± 0.7
K19[d]		−5.171 ± 0.002	−0.075 ± 0.002	0.21 × 0.17 (177)	−4.5 ± 0.5	0.6 ± 0.9
K20	He I-N2/IRS16	2.400 ± 0.002	−0.236 ± 0.001	0.54 × 0.10 (64)	−6.5 ± 0.6	−6.7 ± 0.4
K21[e]		−3.238 ± 0.002	−0.455 ± 0.002	0.28 × 0.21 (125)	−5.7 ± 0.4	10.7 ± 0.5
K22	VISIR60	−1.519 ± 0.002	−0.461 ± 0.003	0.36 × 0.17 (26)	−8.8 ± 0.5	−1.4 ± 1.5
	Source − ε					
K23[e]		−2.922 ± 0.001	−0.902 ± 0.002	0.27 × 0.14 (48)	−1.2 ± 0.2	4.9 ± 0.4
K24	IRS13N-α	−2.642 ± 0.001	−1.415 ± 0.001	0.30 × 0.07 (36)	2.2 ± 0.2	7.1 ± 0.3
K25	IRS33NW	−0.737 ± 0.014	−1.535 ± 0.018	0.36 × 0.21 (144)	−13.4 ± 1.2	16.7 ± 1.9
K26	IRS13E5	−3.402 ± 0.001	−1.551 ± 0.001	0.13 × 0.12 (23)	−5.1 ± 0.2	2.0 ± 0.3
K27	IRS13E3	−3.188 ± 0.001	−1.566 ± 0.001	0.21 × 0.11 (174)	−3.4 ± 0.1	2.6 ± 0.1
K28		0.032 ± 0.001	−1.636 ± 0.002	0.14 × 0.01 (45)	−10.3 ± 0.3	1.8 ± 0.6
K29[f]		−2.846 ± 0.001	−1.778 ± 0.001	0.27 × 0.14 (48)	1.4 ± 0.2	2.5 ± 0.2
K30	IRS13W	−3.999 ± 0.001	−1.851 ± 0.002	0.21 × 0.05 (19)	−3.9 ± 0.3	−1.0 ± 0.5
K31[f]		−3.346 ± 0.001	−1.913 ± 0.001	0.27 × 0.22 (37)	−4.2 ± 0.2	−0.5 ± 0.3
K32	MP-1.70-1.65	−1.766 ± 0.007	−1.951 ± 0.003	0.25 × 0.14 (72)	−15.9 ± 1.6	3.4 ± 1.4
	Source − ζ					
K33	IRS33N	−0.312 ± 0.005	−2.245 ± 0.003	0.60 × 0.22 (113)	−7.7 ± 1.1	0.9 ± 0.7
K34		−4.164 ± 0.001	−2.309 ± 0.003	0.49 × 0.05 (4)	−1.9 ± 0.6	−1.0 ± 0.7
K35		−3.160 ± 0.001	−2.403 ± 0.001	0.34 × 0.12 (22)	−2.9 ± 0.2	4.8 ± 0.4
K36	IRS21	2.365 ± 0.001	−2.648 ± 0.001	0.24 × 0.15 (98)	−2.4 ± 0.4	−1.8 ± 0.5
K37		6.536 ± 0.005	−2.781 ± 0.007	0.46 × 0.20 (29)	0.8 ± 0.6	9.0 ± 0.9
K38		−4.114 ± 0.001	−2.788 ± 0.001	0.23 × 0.01 (150)	−3.3 ± 0.2	3.4 ± 0.3
K39		−5.458 ± 0.004	−2.844 ± 0.004	0.37 × 0.17 (131)	−3.2 ± 0.8	1.6 ± 1.0
K40	XJ174540.0290031	−0.264 ± 0.001	−3.028 ± 0.002	0.12 × 0.01 (92)	−7.1 ± 0.4	10.1 ± 1.9
K41		−1.317 ± 0.001	−3.083 ± 0.003	0.50 × 0.09 (178)	−5.3 ± 0.2	0.6 ± 0.6
K42	MP-1.80-2.95	−1.867 ± 0.001	−3.106 ± 0.002	0.33 × 0.20 (167)	−6.2 ± 0.7	4.4 ± 1.2
	Source − η					
K43[g]		−3.337 ± 0.001	−3.402 ± 0.002	0.99 × 0.23 (3)	−1.9 ± 0.2	2.4 ± 0.5
K45	IRS33E	0.338 ± 0.004	−3.430 ± 0.002	0.48 × 0.13 (77)	−4.6 ± 1.2	−0.9 ± 0.6
K46[g]		−3.771 ± 0.001	−3.433 ± 0.004	0.83 × 0.19 (9)	−6.3 ± 0.3	−1.2 ± 0.8
K47	IRS13SSE	−2.443 ± 0.002	−4.338 ± 0.003	0.43 × 0.17 (22)	−7.4 ± 0.4	1.6 ± 0.6
K48		2.729 ± 0.003	−4.402 ± 0.003	0.30 × 0.21 (88)	−4.1 ± 0.9	1.5 ± 0.7
K49		−1.649 ± 0.003	−4.591 ± 0.016	1.11 × 0.16 (176)	−6.0 ± 0.6	6.7 ± 2.4
K50	IRS9NW	2.909 ± 0.002	−5.056 ± 0.002	0.49 × 0.16 (129)	−4.2 ± 0.5	2.5 ± 0.4
K51		3.709 ± 0.003	−5.191 ± 0.004	0.67 × 0.20 (145)	−4.6 ± 0.8	1.7 ± 1.3
K52	IRS2S	−3.884 ± 0.004	−5.419 ± 0.005	0.39 × 0.31 (10)	−2.5 ± 0.9	−5.8 ± 1.6
K53		−2.817 ± 0.002	−5.434 ± 0.003	0.45 × 0.14 (149)	−4.7 ± 0.4	−2.2 ± 0.6
K54		−2.198 ± 0.003	−5.530 ± 0.003	0.44 × 0.13 (148)	−1.0 ± 0.5	−5.3 ± 0.9
K55		14.575 ± 0.003	−5.629 ± 0.007	0.68 × 0.27 (10)	0.3 ± 1.2	−8.7 ± 2.3
K57	IRS9N	5.683 ± 0.002	−5.728 ± 0.002	0.24 × 0.15 (122)	−2.5 ± 0.7	−0.9 ± 0.8
K58		−4.508 ± 0.004	−5.838 ± 0.003	0.40 × 0.21 (93)	−6.8 ± 1.1	−1.5 ± 1.4
K59		4.908 ± 0.001	−6.183 ± 0.002	0.43 × 0.19 (29)	−1.0 ± 0.3	−4.8 ± 0.5
K60[h]		1.312 ± 0.004	−6.663 ± 0.003	0.48 × 0.17 (65)	−3.2 ± 0.7	−3.1 ± 0.6
K62[h]		1.319 ± 0.001	−7.058 ± 0.001	0.14 × 0.08 (60)	−0.8 ± 0.7	−7.3 ± 0.9
K63		5.789 ± 0.006	−7.736 ± 0.005	0.47 × 0.28 (83)	1.6 ± 1.5	−5.7 ± 1.2
K64		7.155 ± 0.003	−7.763 ± 0.003	0.25 × 0.19 (119)	−3.0 ± 0.5	0.8 ± 0.7
K66	VISIR12	9.980 ± 0.001	−8.917 ± 0.001	0.73 × 0.19 (23)	−1.1 ± 0.4	2.0 ± 0.6
Measurements from 3.5 cm Observations						
X4		7.321 ± 0.003	15.249 ± 0.006	1.26 × 0.43 (163)	2.0 ± 0.4	−1.0 ± 0.7
X6	MP-8.20+7.80	−8.412 ± 0.004	8.390 ± 0.005	Unresolved	7.2 ± 1.0	3.2 ± 0.6
X7	IRS5SE1	10.599 ± 0.002	7.056 ± 0.003	0.50 × 0.30 (53)	−4.4 ± 0.9	−7.0 ± 0.8
X8		19.847 ± 0.005	5.650 ± 0.013	2.8 × 0.3 (20)	−3.0 ± 0.7	−3.1 ± 1.7

Table 2
(Continued)

Source	IR ID	$\Delta\alpha$ (J2000)[a] (arcsec)	$\Delta\delta$ (J2000)[a] (arcsec)	$\theta_{maj} \times \theta_{min}$ (P.A.)[b] (arcsec×arcsec (deg))	μ_α[c] (mas yr^{-1})	μ_δ[c] (mas yr^{-1})
X9	IRS7	−0.077 ± 0.004	5.611 ± 0.004	0.6 × 0.5 (120)	−1.5 ± 1.2	−5.4 ± 0.6
X11		4.928 ± 0.002	4.229 ± 0.004	2.2 × 0.7 (158)	−4.8 ± 0.8	−4.8 ± 1.0
X12	IRS34NW (Bullet)	−3.465 ± 0.005	1.995 ± 0.010	Unresolved	−6.7 ± 0.8	5.1 ± 1.2
X13	MP+5.70+2.40	5.498 ± 0.002	1.714 ± 0.002	Unresolved	−4.7 ± 0.2	−14.0 ± 0.2
X17		16.231 ± 0.004	−3.306 ± 0.004	Unresolved	−2.3 ± 0.6	−7.3 ± 1.4
X18	IRS28/ IRS4	10.611 ± 0.002	−6.034 ± 0.003	1.5 × 0.8 (2)	−2.3 ± 0.3	−0.5 ± 0.5
X19		−19.124 ± 0.007	−7.830 ± 0.008	Unresolved	5.8 ± 1.8	2.8 ± 0.9
X20		10.086 ± 0.001	−8.940 ± 0.001	Unresolved	−0.06 ± 0.14	−0.8 ± 0.2
X21		−15.516 ± 0.003	−10.221 ± 0.003	Unresolved	−4.7 ± 1.2	1.5 ± 0.6
X23		−19.169 ± 0.003	−14.389 ± 0.004	Unresolved	−6.1 ± 1.1	12.8 ± 2.1
X24	MP-09-14.4	−9.180 ± 0.005	−14.680 ± 0.010	Unresolved	−3.5 ± 0.6	−5.4 ± 1.3
X25		−15.366 ± 0.004	−28.188 ± 0.004	Unresolved	−1.7 ± 0.4	3.7 ± 0.5

Notes.
[a] Position offsets with respect to Sgr A*.
[b] Deconvolved source size.
[c] Proper motions.
[d] The radio component is located in the IRS 6/34 region.
[e] The radio component is located in the IRS 13N region.
[f] The radio component is located in the IRS 13E region.
[g] The radio component is located in the IRS 2L region.
[h] The radio component is located in the VISIR 51 region.

3.2.2. Radial Velocity in the Three Mini-spiral Arms

Figure 5(a) shows the image of the integrated H92α line intensity. This clearly delineates the three well known kinematic features of Sgr A West: the Northern Arm, Eastern Arm, and Western Arc. The H92α line spectra at the positions marked by the circles in each of the streams (Figure 5(b)) are shown in Figure 5(c). We determined the kinematic parameters (radial velocity and line-width) from the spectra at these locations using Gaussian fitting. Table 3 summarizes the results. Columns 1, 4 and 7 are the identification of the locations in the three arms. Columns 2, 5 and 8 are the right ascension and declination offsets from Sgr A*. Columns 3, 6 and 9 list the LSR velocity and FWHM line-width of the velocity components from the LSQ fitting.

4. RESULTS

4.1. Three-dimensional Velocities of the Winds from Supergiants IRS 7 and IRS 8

Figure 6 shows the finding chart for the IR sources in the radio image of Sgr A West.

IRS 7. IRS 7 is the brightest near-IR source at the Galactic center, associated with an M supergiant (Wollman et al. 1982; Lebofsky et al. 1982). In our high-angular-resolution map at 1.3 cm (Figure 7(a)), the head of IRS 7 was resolved into several bright components in a shape consistent with a bow shock and a tailed structure $\sim$2″ (0.1 pc) north of the head. The shape of the bow shock is in good agreement with that observed with lower resolution by Yusef-Zadeh & Melia (1992) at 2 cm. The bridge between the head of the bow shock and the emission knot in the tail is resolved out at our resolution of 0.″1 × 0.″2. Figure 7(c) shows the detailed structure of the radio emission from the bow shock.

We overlay the IRS 7-SiO maser position of Reid et al. (2007) and star positions from several IR measurements on the radio images for comparison in Figure 7(a). The IRS 7-SiO maser appears to be surrounded by radio continuum emission in the high-resolution image at 1.3 cm, and agrees with the centroid position of the radio emission in the low-resolution image at 3.6 cm (contours in Figure 7(a)) within an offset $\leqslant$0.″1. The centroid position at 3.6 cm at epoch 2002X is in good agreement with that determined by Yusef-Zadeh et al. (1989) at 2 cm at an early epoch, after correction for proper motion. The positions of the IR star determined in the IR measurements by a number of IR groups (Blum et al. 1996; Genzel et al. 2000; Viehmann et al. 2005) show offsets ($\sim$0.″1–0.″2) from the radio positions (Figure 7(a)). The IRS 7-SiO maser, believed to be located close to the M supergiant (<10 mas), has been used for the position registration in the coordinate frames at IR and radio wavelengths (Menten et al. 1997; Reid et al. 2003, 2007). Therefore, we use the position of the IRS 7-SiO maser measured at 2006.23 (Reid et al. 2007) as the reference position for the star of IRS 7, that is, the IR positions used in this paper have been corrected for the offsets between the position of the IRS 7 star from various published catalogs and that of the IRS 7-SiO maser at 2006.23.

The proper motion of IRS 7, $\mu_\alpha = -1.5 \pm 1.2$ mas yr^{-1} and $\mu_\delta = -5.4 \pm 0.6$ mas yr^{-1} at epoch 2002X, was determined from the four epochs' data at 3.6 cm, giving $V_x = -56 \pm 44$ km s^{-1} and $V_y = -205 \pm 21$ km s^{-1}, well agreeing with the proper motion of the IR star from Genzel et al. (2000). The radial velocity determined from the H92α line is $V_{LSR} = -123 \pm 7$ km s^{-1} (Figure 7(b)), which is in good agreement with that derived from [Ne II] emission line (Serabyn et al. 1991). The total velocity of the ionized gas, $V = \sqrt{V_x^2 + V_y^2 + V_{LSR}^2} = 246 \pm 20$ km s^{-1}, agrees with the results measured from the SiO maser within 3σ (Reid et al. 2007). Based on the cometary morphology, Yusef-Zadeh & Morris (1991) proposed that the radio structure (Figure 7(c)) is caused by the ram pressure of a nuclear wind or by radiative pressure arising from the IRS 16 cluster of stars surrounding Sgr A*. The current

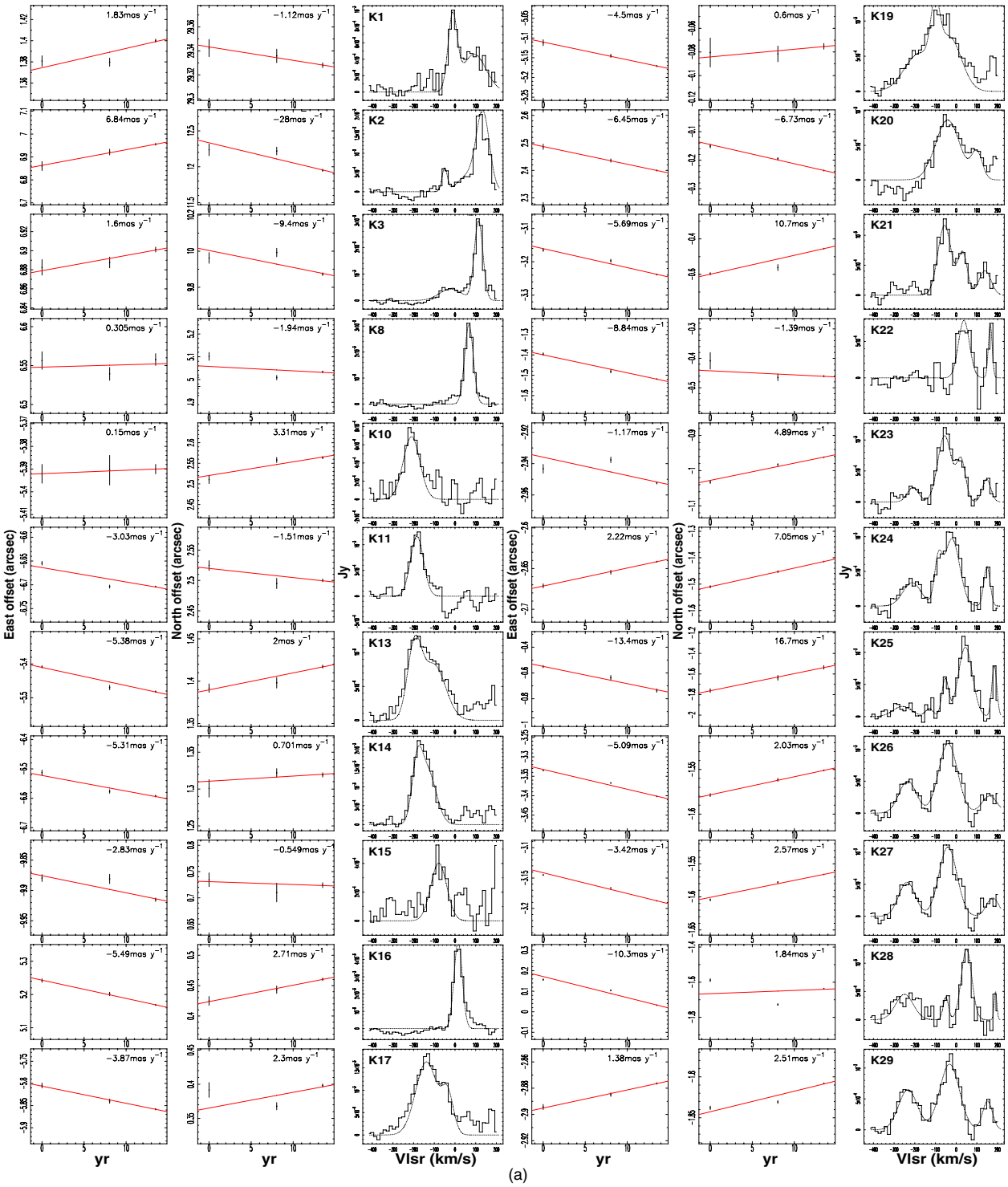

Figure 3. Plots of the eastward (Columns 1 and 4) and northward (Columns 2 and 5) position offsets from Sgr A* vs. time, and the H92α line spectra (Columns 3 and 6) in the LSR for 70 H II components. The component IDs are labeled (top left) on each H92α line spectrum panel. The uncertainty (1σ) in position offsets is marked with a vertical bar. The linear LSQ fitting (red) to the position offsets weighted by σ^2 was used to determine the slope (proper motions) of the displacements. The proper motion determined are labeled in each of the corresponding panels. The LSQ fitting to the spectra with multiple Gaussians (dashed curves) was used to determine the radial velocities of each component. The results are summarized in Table 2.

(A color version of this figure is available in the online journal.)

observations agree with the models discussed by Yusef-Zadeh & Morris (1991) and Yusef-Zadeh & Melia (1992).

IRS 8. IRS 8 was detected at 2.2 μm by Becklin & Neugebauer (1975), with an estimated luminosity $\sim 1 \times 10^5 L_\odot$. The bow-shock structure of radio continuum emission in the high-resolution image of IRS 8 at 1.3 cm (Figure 8) is in excellent agreement with the IR structure and the location of the IRS 8 star at $\Delta\alpha = 1''.2$ and $\Delta\delta = 29''.3$ (Geballe et al. 2004). The position of the radio continuum peak agrees with that of the IR apex in the bow shock.

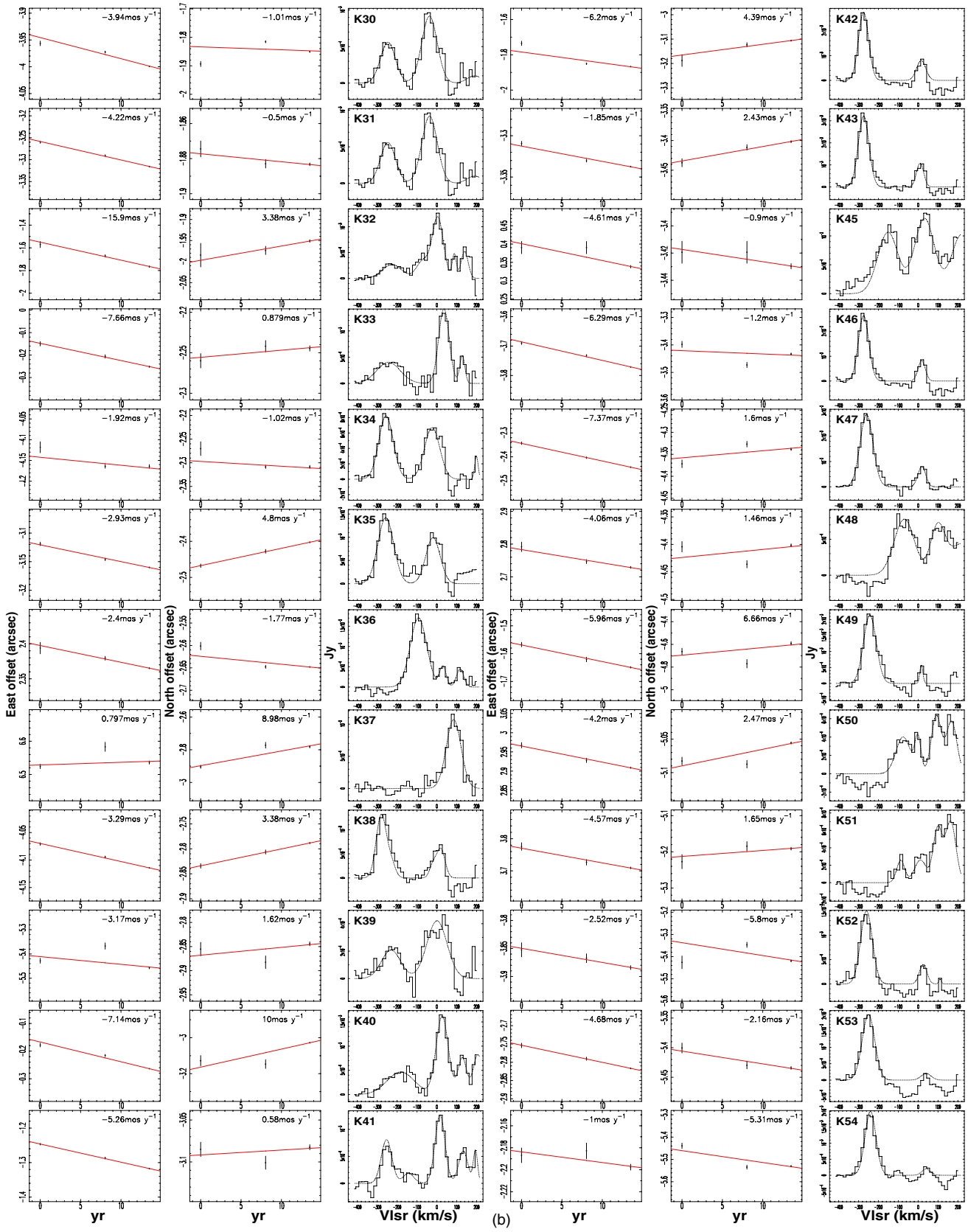

Figure 3. (Continued)

The proper motion of the radio peak is measured to be $\mu_\alpha = 1.8 \pm 0.3$ mas yr^{-1}, $\mu_\delta = -1.1 \pm 0.5$ mas yr^{-1}, or $V_t = \sqrt{V_x^2 + V_y^2} = 80 \pm 14$ km s^{-1} (P.A. $= 121^\circ \pm 24^\circ$).

In the lower resolution ($\theta_{\rm FWHM} = 2''$) channel image in H92α, a symmetrical line emission has been detected at -10 km s^{-1} in the IRS 8 region. We integrated the velocity from -25 to 5 km s^{-1} to show the integrated-line-flux image (contours in

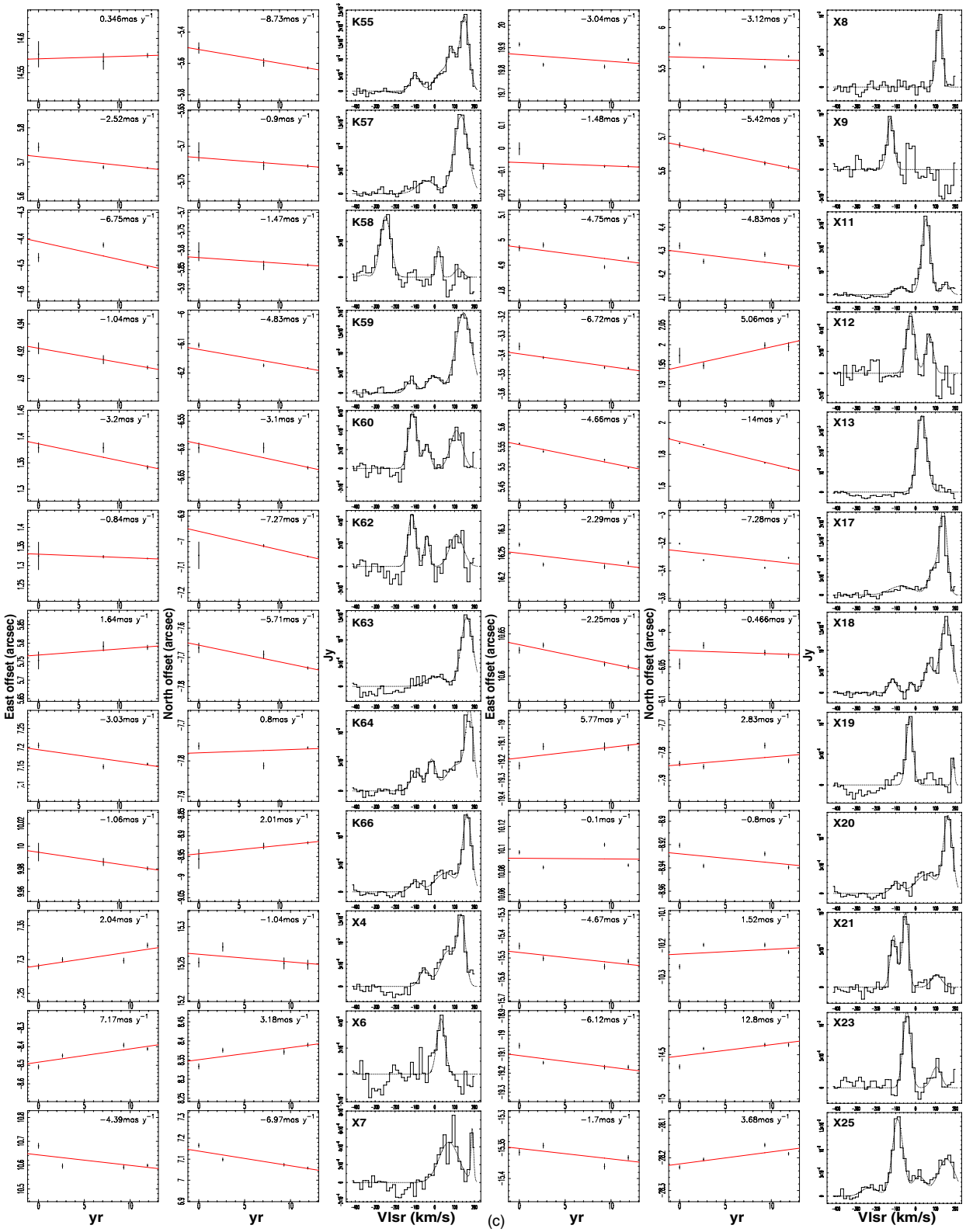

Figure 3. (Continued)

Figure 9(a)). We refer to this structure, which has a size of 5″ (EW) by 6″ (NS; blue), as the "IRS 8 nebula" since its radial velocity is consistent with that of the IRS 8 star (Geballe et al. 2006). In Figure 9(a), the IRS 8 nebula is compared to the pseudo-color image of the integrated-line emission from the Northern Arm in the velocity range of 35–170 km s^{-1}. The intensity-weighted velocity images are also shown in Figure 9(b), for the negative-velocity gas in the IRS 8 nebula. Figure 9(c) shows the intensity-weighted velocity distribution of the redshifted gas in the Northern Arm. A high-spatial-resolution (1.″25) spectrum in Figure 9(d) was created from region 1 with the dominant line emission at -18 ± 4 km s^{-1}

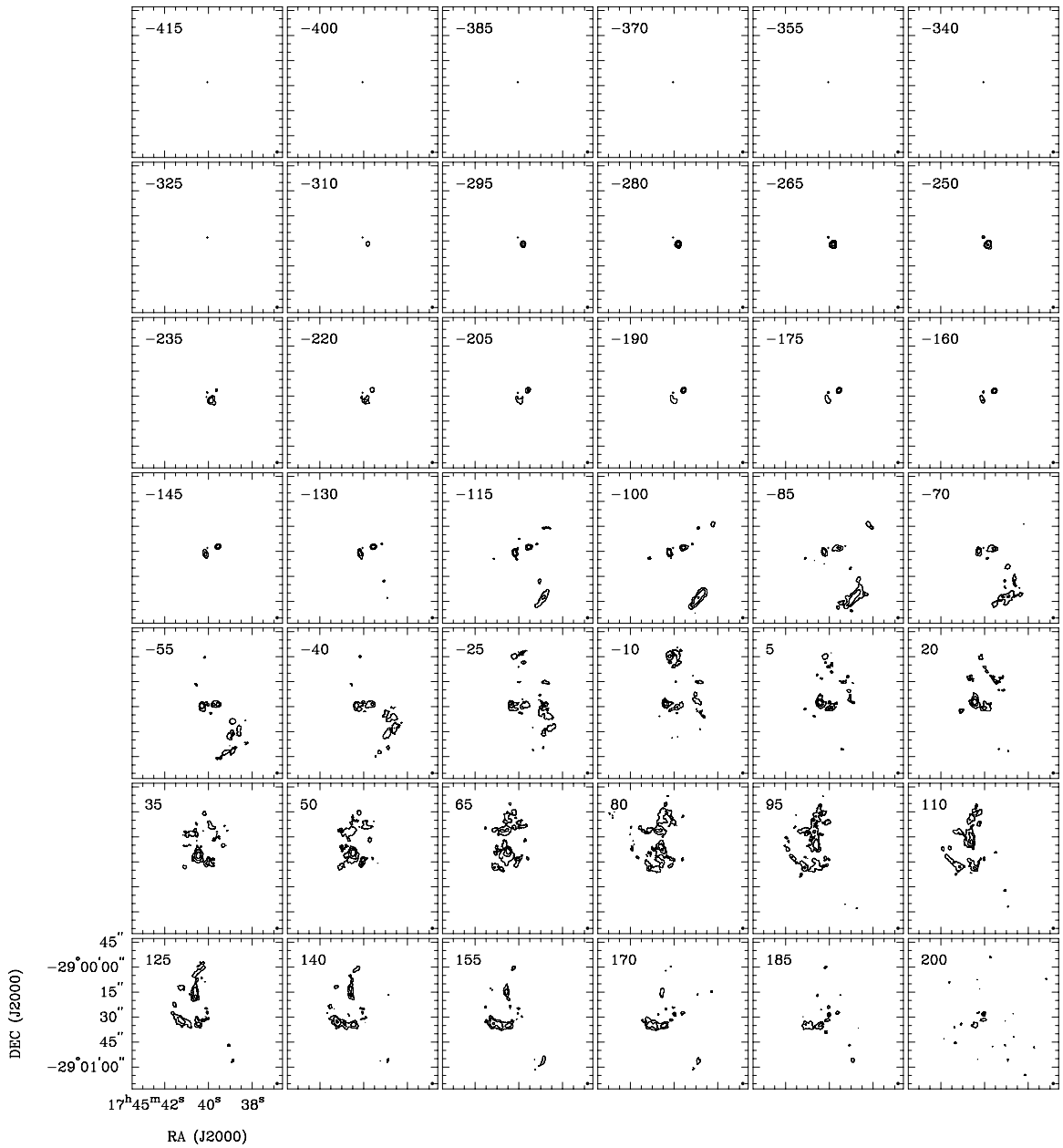

Figure 4. Channel images of the H92α line convolved with a circular beam of 2″. The contours are 0.27 mJy beam^{-1} × (–5, 5, 10, 20, 40, 80, 160). The LSR velocities (–415 to +200 km s^{-1}) are labeled in each of the channel images. The rms is in the range 0.15–0.27 mJy beam^{-1}.

from the IRS 8 nebula and much weaker line emission from the Northern Arm. A spectrum of the line emission at 87 ± 7 km s^{-1} from region 3 in the Northern Arm is shown in Figure 9(e). In Figure 9(f), the spectrum (black) from region 2 is compared to the spectrum (red) from the position of the radio continuum peak in the bow shock. The H92α spectra in the bow-shock region show both a broad, redshifted feature at $V_{\rm LSR} = 80 \pm 28$ km s^{-1} with $\Delta V_{\rm FWHM} = 137 \pm 53$ km s^{-1} and a somewhat narrower feature at $V_{\rm LSR} = -14 \pm 5$ km s^{-1} with $\Delta V_{\rm FWHM} = 52 \pm 17$ km s^{-1}. The H92α line spectra in the shocked region agree with the spectrum of [Ne II] at IRS 8 in a larger area (Geballe et al. 2004). Furthermore, a comparison of H92α line spectra shows that line emission from region 2 (in the tail of the IRS 8 bow shock) is a factor of 1.5 stronger than that from the position at the continuum peak (the head of the IRS 8 bow shock). We derived line-to-continuum ratios (L/C) of 5% ± 1% and 2.5% ± 0.5% from the tail and head of the bow shock, respectively. The significant difference in L/C between the head and the tail suggests that the local thermodynamic equilibrium (LTE) electron temperature in the head ($T_e \sim 1.3 \times 10^4$ K) is higher than that in the tail ($T_e \sim 7.0 \times 10^3$ K), if the gas is optically thin. The suggested higher electron temperature in the head of the bow shock may result from a strong shock interaction of the IRS 8 nebula with gas in the Northern Arm. Figure 9(a) also shows that at the position of region 2, both the positive-velocity emission from the Northern Arm (color) and the negative-velocity emission from the IRS 8 nebula (contours) are enhanced, possible evidence that the ionized gas in both the velocity components may be compressed due to their collision. If the interaction can be verified with improved data, we would conclude that both the IRS 8 star and the nebula are located close to the Northern Arm and approach the mini-spiral arm from the

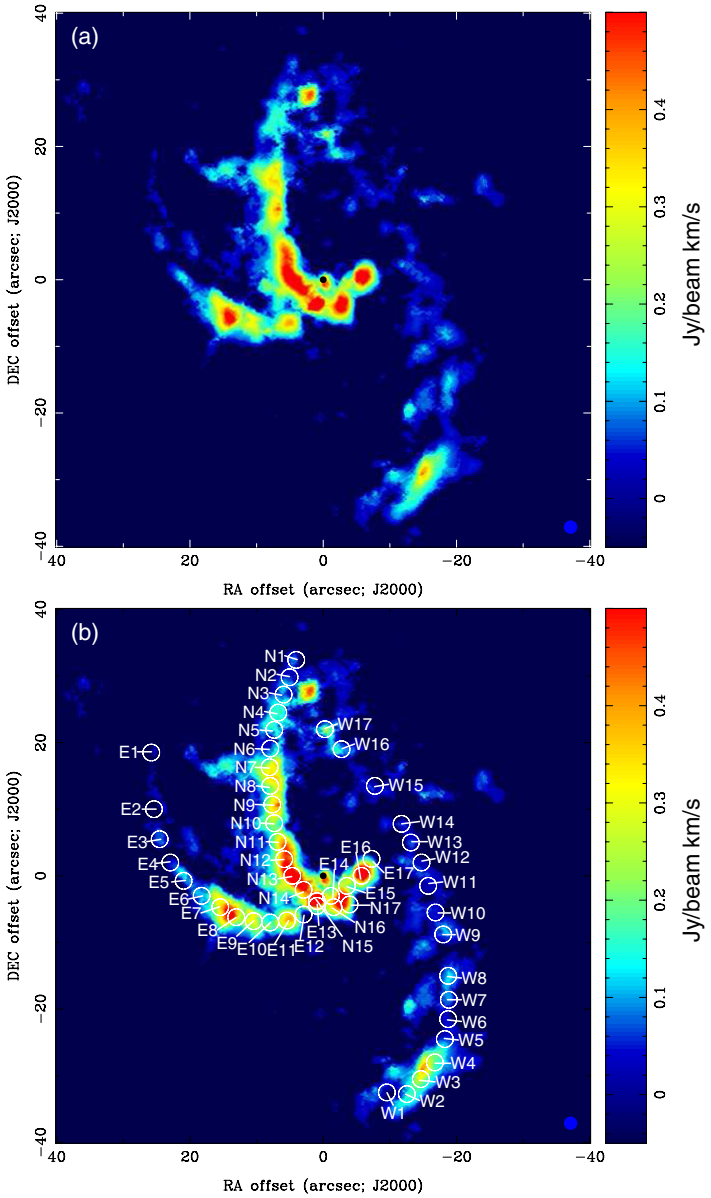

Figure 5. ((a) and (b)) Integrated H92α line intensity image scaled (in color). The FWHM beam (right bottom) is 2″. The solid dot in the images marks the position of Sgr A*. The locations of the spectra shown in (c) are marked with the white circles in (b) and their positions are tabulated in Table 3. (c) Spectra from a sequence of locations (marked in (a)) in each of the arms. The red curves are the LSQ fits with multiple Gaussians. The blue bars indicate the observed peak velocity of the kinematic components for the corresponding streams. The measurements of radial velocities are summarized in Table 3.

far side with respect to Sgr A* considering their opposite radial velocities.

Figure 9(g) shows a spectrum toward IRS 8 nebula, integrated over a region of size $6'' \times 5''$ (P.A. $= 0°$) centered at an offset from Sgr A* of $\Delta\alpha = -1\farcs19$, $\Delta\delta = 26\farcs3$. The IR star is located $\sim 4''$ NE of the nebula center. We fit two Gaussian components to the integrated spectrum, giving $S_{\rm L} = 34 \pm 5$ mJy, $V_{\rm LSR} = -12$, $\Delta V_{\rm FWHM} = 46 \pm 20$ km s^{-1} from the IRS 8 nebula and $S_{\rm L} = 26 \pm 4$ mJy, $V_{\rm LSR} = 75 \pm 24$ km s^{-1}, $\Delta V_{\rm FWHM} = 122 \pm 50$ km s^{-1} from the Northern Arm stream. The two components are clearly separated in the integrated spectrum. For the IRS 8 nebula (the negative-velocity component), the emission measure (EM $\approx 8 \times 10^6$ cm^{-6} pc) and the mean electron density ($n_e \approx 6 \times 10^3$ cm^{-3}) are inferred assuming that the H92α line is optically thin. Based on the derived excitation parameter ($U \approx 35$ cm^{-2} pc), the rate of ionizing photons ($N_{\rm Lyc} \approx 1.5 \times 10^{49}$ phot. s^{-1}) is inferred on the assumption that only 10% of the Lyman continuum flux contributes to ionizing the IRS 8 nebula owing to the fact that the ionizing star is located on the edge of the nebula. Thus, the ionizing source of the IRS 8 nebula is equivalent to an O5.5-6 zero-age main sequence (ZAMS) star (Panagia 1973), which agrees well with the spectral type inferred from the IR spectrum (Geballe et al. 2006). The location of the IRS 8 star with respect to the edge of the nebula, displaced by 4″ (~0.15 pc) from the center, is striking. This displacement suggests that the star runs away from the progenital ionized cloud (as delineated by the blue contours in Figure 9(a)) into a dense medium, the Northern Arm (as scaled with color in the same figure). The shape and the location of the observed bow shock with respect to the IR star also agree with this scenario. The velocity of the star is probably similar to the bow-shock velocity, that is, $V_{\rm bs} \sim \Delta V_{\rm FWHM} = 46$ km s^{-1} with respect to the nebular center which is at a velocity of ~0 km s^{-1}. The observed transverse velocity $V_{\rm t} = 80 \pm 16$ km s^{-1} (P.A. =

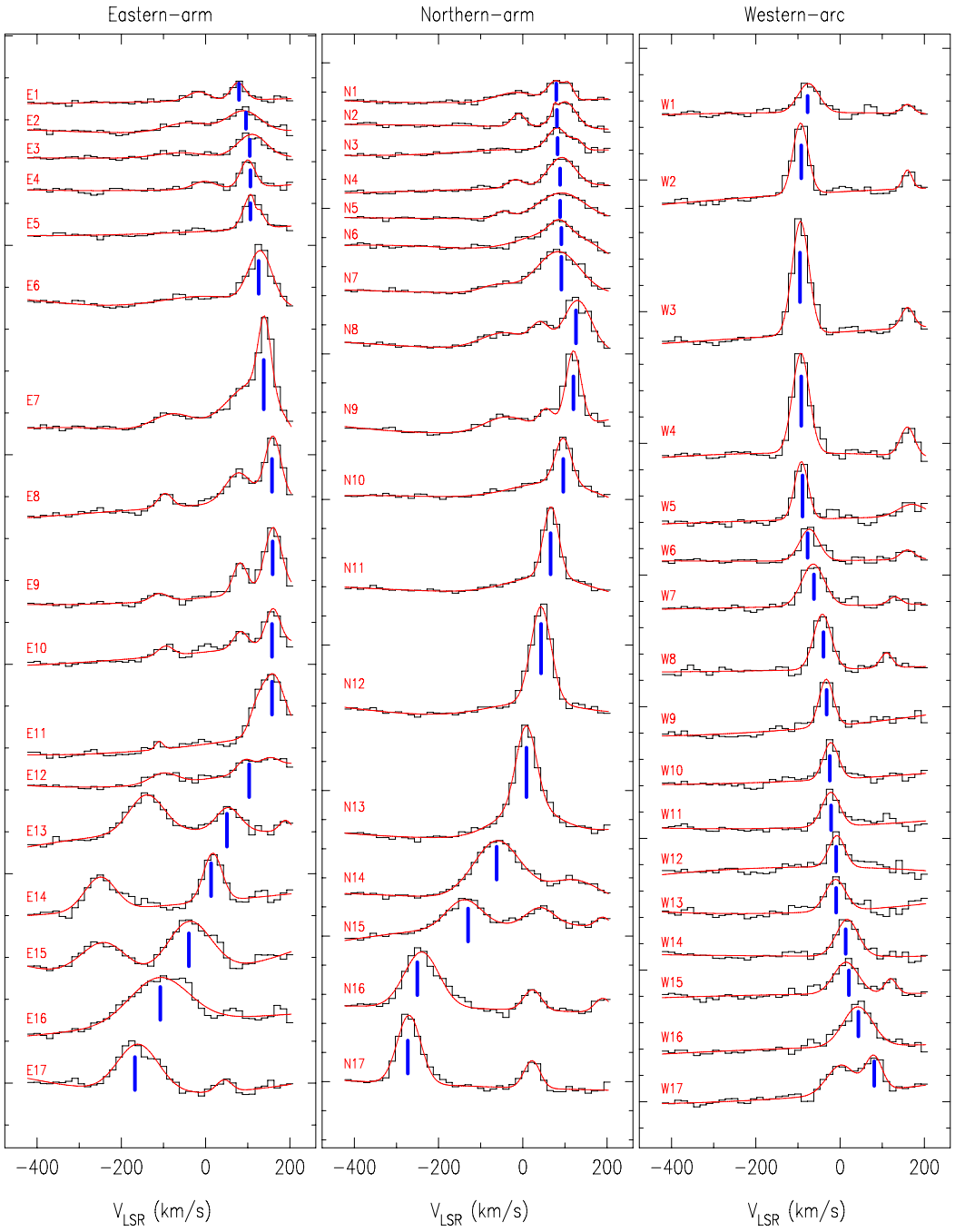

Figure 5. (Continued)

121° ± 25°) from our proper motion measurement of the apex corresponds to the velocity of the medium flow in the Northern Arm shocked by the stellar wind from IRS 8. The time for the star to move from the center to the edge of the nebula would be $>3 \times 10^3$ yr if the star has the same velocity as that of the bow shock ($V_{\rm bs}$).

4.2. Motions of the Sources in the Northern Arm

IRS 5SE1. A bright radio source, X7 ($S \sim 7$ mJy at 3.6 cm), can be identified in the IRS 5 field. Within the errors, this source agrees with the mid-IR position of IRS 5SE1 of Viehmann et al. (2005; we note that the IR position reported by Perger et al. 2008 is offset by more than 1″ from X7). The radio emission X7 is resolved at 1.3 cm (Figures 10(a) and 22) showing a triangular structure 0.″5 in size pointing toward Sgr A*. The radio morphology of IRS 5SE1 agrees with the structure of the dust tail observed in the L' band by Perger et al. (2008). The proper motion data of X7 at 3.6 cm suggest that the source moves toward the southwest (SW) with a transverse velocity of $V_{\rm t} = 313 \pm 31$ km s^{-1} (P.A.$= -148° \pm 7°$), nearly perpendicular to the proper motion vector of IRS 5SE1 determined from 2.18 μm astrometry (Perger et al. 2008). The H92α line spectrum shows a spatially extended, broad spectral feature at $V_{\rm LSR} = 72 \pm 16$ km s^{-1} with $\Delta V_{\rm FWHM} = 116 \pm 41$ km s^{-1} (Figure 3(c)). The radial velocity is consistent with the velocity of the Northern Arm but the transverse velocity is two times larger. Based on the radio observations, IRS 5SE1 appears to run into the Northern Arm.

Table 3
Radial Velocities from Three Mini-spiral Arms

ID[a]	$\Delta\alpha, \Delta\delta$[b] (arcsec)	$V_{\rm LSR}, \Delta V_{\rm FWHM}$[c] (km s^{-1})	ID[a]	$\Delta\alpha, \Delta\delta$[b] (arcsec)	$V_{\rm LSR}, \Delta V_{\rm FWHM}$[c] (km s^{-1})	ID[a]	$\Delta\alpha, \Delta\delta$[b] (arcsec)	$V_{\rm LSR}, \Delta V_{\rm FWHM}$[c] (km s^{-1})
Northern Arm			Eastern Arm			Western Arm		
N1	4.05, 32.40	78, 45	E1	25.00, 18.5	77, 40	W1	−9.55, −32.50	−75, 59
N2	5.05, 29.80	100, 61	E2	24.15, 10.0	91, 92	W2	−12.55, −32.75	−94, 42
N3	5.95, 27.20	82, 54	E3	23.15, 5.50	110, 80	W3	−14.65, −30.50	−94, 47
N4	6.75, 24.50	92, 75	E4	21.55, 2.00	100, 40	W4	−16.75, −28.00	−93, 47
N5	7.35, 21.90	92, 129	E5	19.75, −0.75	110, 45	W5	−18.25, −24.50	−92, 38
N6	7.95, 19.10	100, 214	E6	17.55, −3.0	130, 66	W6	−18.75, −21.50	−73, 54
N7	8.05, 16.30	84, 120	E7	15.25, −4.7	140, 35	W7	−18.85, −18.60	−64, 64
N8	7.95, 13.50	130, 78	E8	13.05, −6.2	160, 45	W8	−18.75, −15.00	−42, 49
N9	7.65, 10.70	120, 42	E9	10.45, −6.80	160, 47	W9	−18.00, −8.80	−33, 40
N10	7.35, 7.90	96, 45	E10	7.95, −7.00	160, 40	W10	−16.85, −5.50	−22, 42
N11	6.85, 5.10	67, 42	E11	5.45, −6.70	120, 40	W11	−15.75, −1.50	−22, 49
N12	5.85, 2.50	43, 57	E12	2.95, −5.80	93, 45	W12	−14.75, 2.00	−8, 45
N13	4.65, 0.00	8, 57	E13	0.95, −4.50	54, 66	W13	−13.15, 5.00	−11, 57
N14	2.95, −2.10	-60, 131	E14	−1.15, −3.00	−17, 52	W14	−11.75, 7.80	17, 61
N15	0.95, −3.80	−140, 97	E15	−3.55, −1.50	−39, 125	W15	−7.75, 13.50	20, 68
N16	−1.55, −4.70	−240, 97	E16	−5.75, −0.00	−110, 165	W16	−2.75, 19.00	52, 82
N17	−3.95, −4.30	−270, 66	E17	−7.55, 2.25	−160, 115	W17	−0.25, 22.00	90, 47

Notes.
[a] IDs of locations in the mini-spiral arms.
[b] Position offsets from Sgr A*.
[c] The LSR velocity and FWHM velocity width of the spectral features.

IRS 10W. IRS 10W is located in the Northern Arm. A shell-like radio continuum source (K8 in Figure 10(b)) is revealed in the high-resolution image at 1.3 cm, suggesting an association with a bow shock. We note that the orientation of the radio bow shock appears to be very different (by ∼120°) from that determined from the near-IR observations (Tanner et al. 2005). The apex of the radio bow-shock emission appears to be located SW with respect to the mid-IR source IRS 10W (Viehmann et al. 2005). Proper motion measurements of the radio bow shock imply a southward motion of $V_{\rm t} = 73 \pm 30$ km s^{-1} (P.A.= 171° ± 20°). The H92α line spectrum at K8 shows a prominent line emission feature at $V_{\rm LSR} = 67 \pm 2$ km s^{-1} with $\Delta V_{\rm FWHM} = 49 \pm 4$ km s^{-1} (Figure 3(a)), suggesting that this radio source is associated with the Northern Arm.

IRS 21. In the high-resolution 1.3 cm radio image, the core of the ionized gas surrounding IRS 21 is resolved with a deconvolved size of 0.″24 × 0.″15 (P.A. = 98°) and a total flux density of 9.0 ± 0.5 mJy (Figure 10(c)); the source is slightly resolved at 3.6 cm with a total flux density of 10 ± 1 mJy. The measurements are consistent with a free–free origin of the radio emission from the externally ionized winds of the IRS 21 star. The morphology of the ionized gas appears to be in good agreement with the dust emission structure observed in the IR bands (Tanner et al. 2002). The proper motion measurements suggest that the radio source (K36) of IRS 21 moves SW with a transverse velocity of $V_{\rm t} = 114 \pm 17$ km s^{-1} (P.A.= −127° ± 15°). The H92α line spectrum (K36 in Figure 3(c)) shows a radial velocity of $V_{\rm LSR} = -92 \pm 4$ km s^{-1} with $\Delta V_{\rm FWHM} = 97 \pm 10$ km s^{-1}. The moving direction of the radio source K36 appears to be similar to that of the Northern Arm gas at this location ($V_z = -130$ km s^{-1}, $V_{\rm t} = 401$ km s^{-1} with P.A.= −132°) as predicted from the Keplerian model (see Section 5) but the magnitude of the total velocity appears to be significantly less than (by a factor of ∼3) the model values. This discrepancy suggests that the radio source K36 of IRS 21 might be in an orbit significantly different from that of the Northern Arm.

CXOGC J174540.029003. This X-ray transient was discovered by the *Chandra X-ray Observatory* (Muno et al. 2005; Porquet et al. 2005), while a double radio source was found to be associated with the X-ray source (Bower et al. 2005). The double radio source (at the 2005 epoch during the burst) is shown in Figure 10(f). The SW component was present in all three epochs with varying flux densities of 1.1 ± 0.1, 1.1 ± 0.1, and 3.4 ± 0.1 mJy in 1991K, 1999K, and 2005K, respectively. The position of the SW component agrees with the X-ray source within the uncertainties, suggesting that this component is associated with that of the X-ray source, presumably a low-mass X-ray binary. The northeast (NE) component was present only in the 2005K epoch with flux density 3.5 ± 0.1 mJy and was not detected at the 3σ level of 0.11 and 0.14 mJy beam^{-1} in the 1999K and 1991K images, respectively; this suggests that the NE component was a hot spot associated with the head of the jet ejected from the persistent, radio-variable star. The SW component shows a large proper motion, with the transverse velocity of $V_{\rm t} = 468 \pm 60$ km s^{-1} (P.A. = −35° ± 6°) toward the northwest (NW) (Figure 10). The radial velocity of the gas in this direction, as determined from the H92α line data, is $V_{\rm LSR} = -182 \pm 19$ km s^{-1}. Both the value of radial velocity and the vector of a transverse velocity are consistent with the velocity predicted in the numerical model for the Northern Arm stream (see Figures 21(b) and (c) and Section 5). Of course, there are no reasons that the X-ray transient CXOGC J174540.029003 should share the motion of the Northern Arm. The agreement between the transverse velocity of the radio source associated with the X-ray transient and the kinematics of the gas in the Northern Arm might be just a coincidence. Also, the X-ray transient is shown to be located within 0.″15 (1σ) of IRS 33SW (marked with a plus in Figure 10(f)), which was detected in the mid-IR (Viehmann et al. 2005). The positional error (±0.″15) in the mid-IR appears to be large. The position coincidence between the X-ray transient and the mid-IR source deserves to be further investigated.

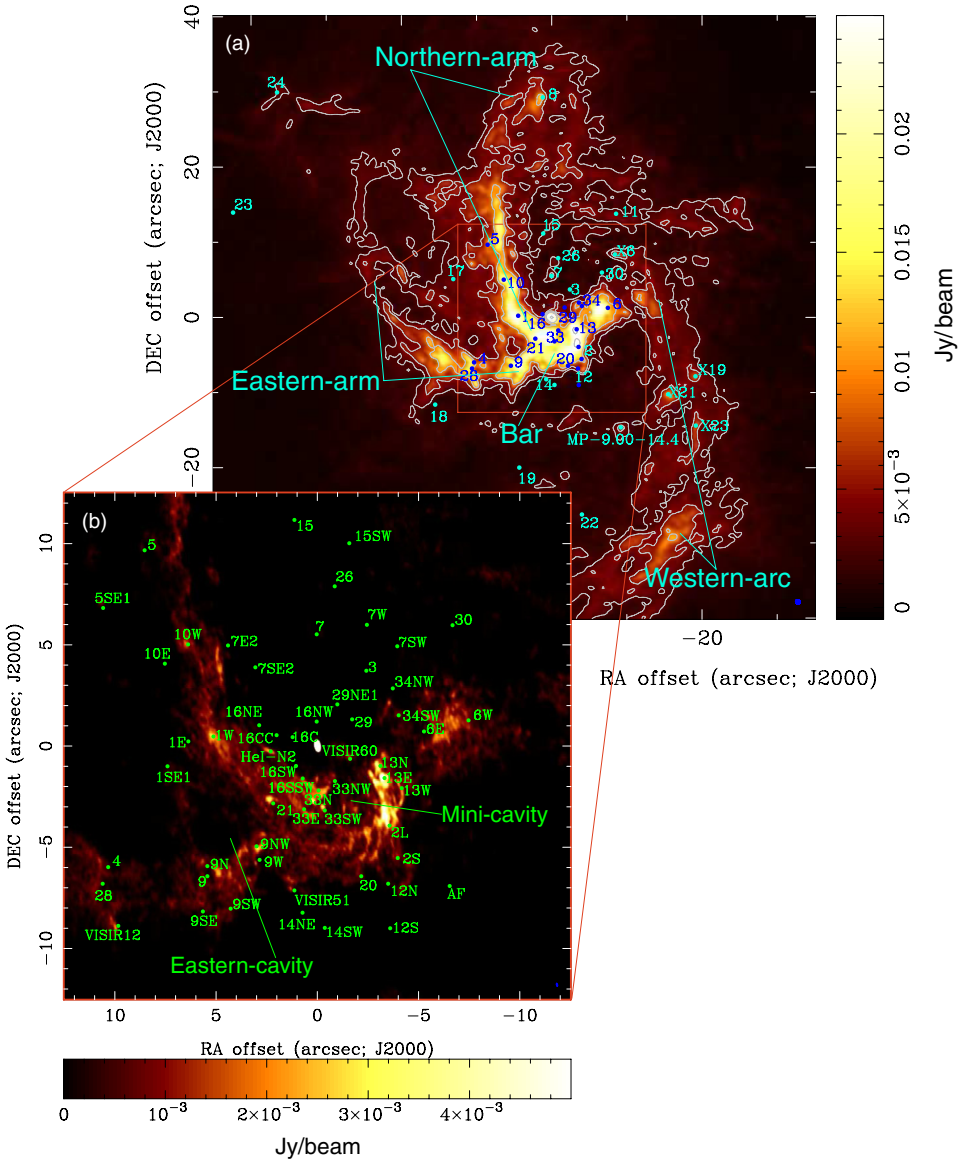

Figure 6. Finding chart of IR sources at the Galactic center. (a) The VLA image (FWHM = 0.″70 × 0.″57, P.A. = 57°) shows the radio emission at 3.6 cm from Sgr A West. Contours are 2.5 mJy beam^{-1} ×(1, 2, 4, 16, 256). (b) The inset of the VLA image (FWHM=0.″2 × 0.″1, P.A. = 11°) shows the inner 20″ region of radio emission at 1.3 cm. The dots mark the IRS positions along with IRS ID numbers (Blum et al. 1996; Genzel et al. 2000; Geballe et al. 2006; Paumard et al. 2004, 2006; Viehmann et al. 2005).

Assuming that the NE component was ejected from the X-ray source located at K40, a proper motion of $\mu_\alpha > 89$ mas yr^{-1} and $\mu_\delta > 58$ mas yr^{-1} is inferred, that is, the velocity of the NE component with respect to K40 is >4000 km s^{-1}. The jet velocity ejected from the radio transient is about an order of magnitude greater than its orbital velocity of ∼500 km s^{-1} in this region, as observed and predicted from the orbital model for the Northern Arm (see Figure 21(c)).

4.3. The Sources in the Eastern Arm

Figure 11 shows the radio components in the Eastern Arm. One of the striking radio features in the Eastern Arm is the arc at $\Delta\alpha = 10.''6$ and $\Delta\delta = -6.''0$ with a width of 0.″2 and a length of at least 3″ (Figure 11(a)). The same morphology is observed at both 1.3 and 3.6 cm (Figures 1, 2 and 6). The IRS 28/IRS 4 star is located close to the location where this radio arc is bent. The structure is resolved at 1.3 cm and proper motion measurements at this wavelength give a large uncertainty; therefore, we use the 3.6 cm data for our reported proper motion measurements. The proper motion derived from the radio component X18 near the center of the arc indicates that it moves westward at $V_t = 89 \pm 12$ km s^{-1} (P.A.= $-102° \pm 56°$). At this location, the radial velocity is $V_{LSR} = 154 \pm 4$ km s^{-1}. These gas motions contrast with those of the star IRS 28: $V_t = 215$ km s^{-1} (P.A. = $159° \pm 4°$) and $V_{LSR} = -55$ km s^{-1} determined from the observations of the SiO maser (Reid et al. 2007). Thus, the ionized gas and the evolved star are probably unrelated. On the other hand, an He I star (He I 17) in the IRS 4 region shows a broad line profile ($\Delta V_{FWHM} \sim 500$ km s^{-1}) centered at $V_{LSR} \sim 130$ km s^{-1} (Krabbe et al. 1991), which agrees with that of X18. We raise the possibility that the high-velocity wind from He I 17 has shocked the ambient gas in the Eastern Arm, and has thereby produced the arc of radio emission.

The component K66 appears to be associated with the mid-IR source VISIR 12 (Viehmann et al. 2005), showing an arc-like structure with an NW proper motion, $V_t = 87 \pm 20$ km s^{-1} (P.A.= $-29° \pm 13°$) and $V_{LSR} = 163 \pm 4$ km s^{-1} (Figure 11(c)). The H92α line shows a radial velocity gradient of 5 km s^{-1}

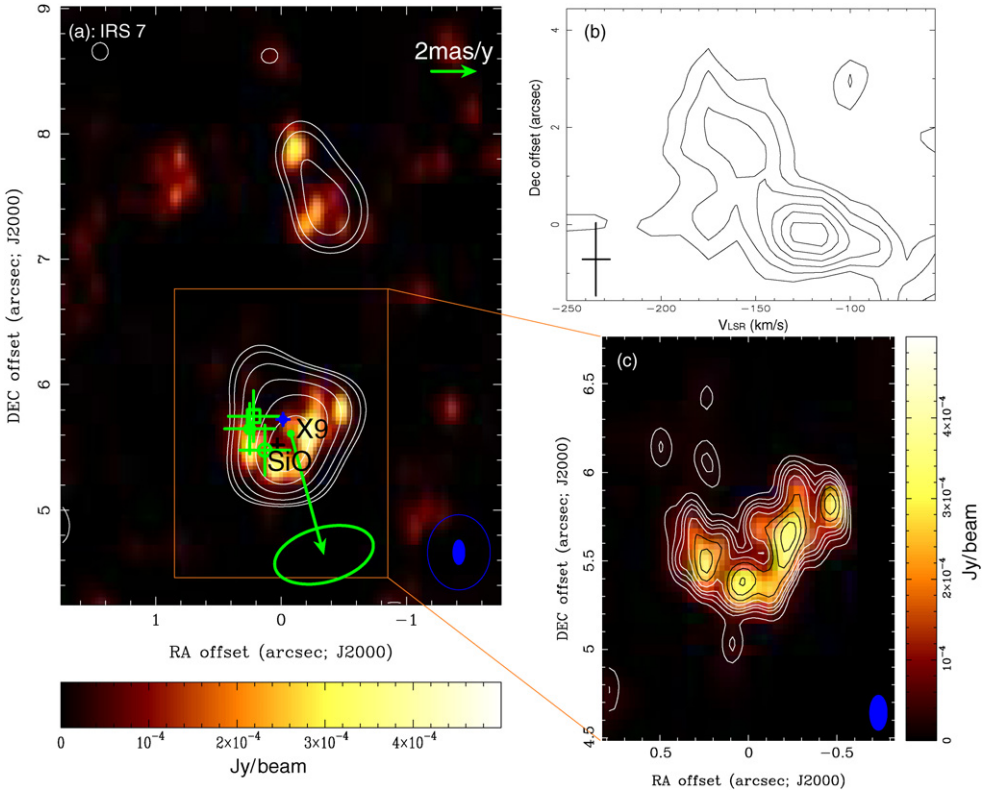

Figure 7. (a) Image of IRS 7 at 3.6 cm (contours, at epoch 2002X) and 1.3 cm (color scale, at epoch 2005 K). Contours are 0.15 mJy beam$^{-1}\times$ (3, 4, 6, 9, 13, 18). The FWHM beams are shown at bottom right for 3.6 cm (empty ellipse, 0.″6 × 0.″5, P.A. = 0°) and 1.3 cm (solid ellipse, 0.″2 × 0.″1, P.A. = 0°). The proper motion vector of X9 is shown with the scaling vector of 2 mas yr^{-1} at top right. The 2σ uncertainty in the proper motion is scaled with the open ellipses for magnitude (the semi-axes along the vector) and direction (the semi-axes perpendicular to the vector). The coordinates are the position offsets from Sgr A*. The green plus signs mark the IR positions obtained from various groups: open circle from Blum et al. (1996), open square from Genzel et al. (2000), and dot from Viehmann et al. (2005). The blue plus dot marks the radio position from Yusef-Zadeh et al. (1989) converting B1950 coordinates to J2000. The black plus marks the position of the SiO maser (Reid et al. 2007). (b) The velocity vs. declination diagram (H92α) along the declination cut across the position of X9 (IRS 7) given in Table 2. The plus sign (bottom left) indicates the FWHM beam size in declination and the channel width in velocity. Contours are 0.15, 0.31, 0.46, 0.62, 0.77, and 0.93 mJy beam^{-1}. The coordinate in declination in the PV diagram is the position offset from X9. (c) Inset of IRS 7 bow shock at 1.3 cm. Contours are 44, 66, 88, 132, 198, 286, 396 μJy beam^{-1}.

per arcsec across this feature. There is no obvious velocity discontinuity. It is possible that K66 is a continuation of the arc feature described above.

In the IRS 9 region, there are two "head–tail" radio components (K57 and K59) located NE and SW of the IR star (IRS 9N) (Figure 11(b)), which is located at the southern rim of the Eastern cavity (Zhao & Goss 1998). Both radio components move generally SW, with $V_{\rm t} = 101 \pm 27$ km s^{-1} (P.A.$= -110^\circ \pm 50^\circ$) and 186 ± 19 km s^{-1} (P.A.$= -168^\circ \pm 4^\circ$) for K57 and K59, respectively. The radial velocities of $V_{\rm LSR} = 133 \pm 4$ km s^{-1} and 145 ± 4 km s^{-1} from the H92α observations are consistent with the values measured from other lines such as Br-γ (Paumard et al. 2004), but differ greatly from that of the IRS 9-SiO maser: -342 km s^{-1} (Reid et al. 2007), suggesting that IRS 9 is not associated with the Eastern Arm.

The radio complex (K48, K50, and K51) may well be associated with IRS 9NW (Figure 11(d)). The mean proper motion of the complex is $\overline{\mu}_\alpha = -4.25 \pm 0.38$ mas yr^{-1} and $\overline{\mu}_\delta = 2.15 \pm 0.34$ mas yr^{-1}, implying $\overline{V}_{\rm t} = 181 \pm 14$ km s^{-1} (P.A.$= -63^\circ \pm 9^\circ$). The H92α line spectra (Figure 3(b)) show multiple velocity components at $V_{\rm LSR} = -70 \pm 15$ km s^{-1} and 98 ± 92 km s^{-1} from K48, $V_{\rm LSR} = -76 \pm 22$ km s^{-1} and 91 ± 15 km s^{-1} and 163 ± 21 km s^{-1} from K50, and $V_{\rm LSR} = 98 \pm 20$ km s^{-1} and 163 ± 21 km s^{-1} from K51, suggesting the presence of more than one velocity stream along the line of sight. We also note that any redshifted components at $V_{\rm LSR} > 200$ km s^{-1} would not be covered by the observations.

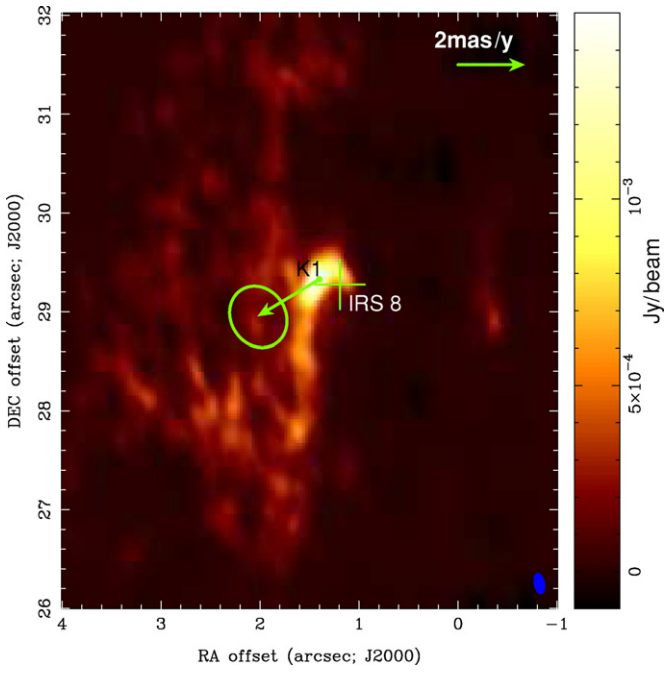

Figure 8. Image of the IRS 8 bow shock (K1) at 1.3 cm and the proper motion vector (scaled with the vector of 2 mas yr^{-1} at top right). The color wedge scales radio intensity in units of Jy beam^{-1}. The FWHM of the beam is 0.″21 × 0.″11 (P.A. = 11°). The semi-axes of the open ellipse scale the 2σ uncertainty of the proper motion. The plus sign is the star position of IRS 8 (Geballe et al. 2006).

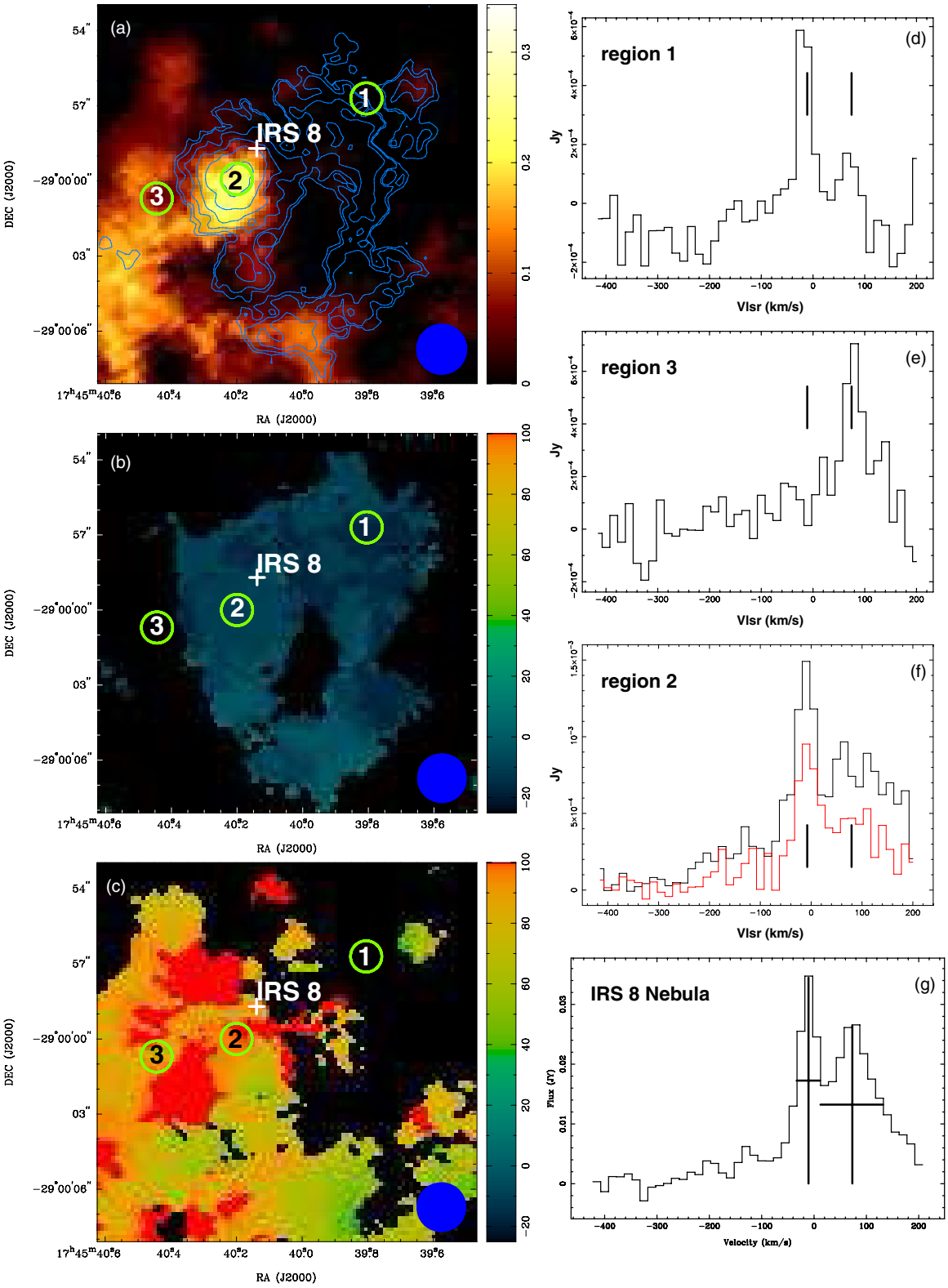

Figure 9. Gas dynamics toward IRS 8. (a) Blue contours show the H92α recombination line intensity integrated from -25 to 5 km s^{-1} (contours: 5 mJy beam^{-1} km s^{-1} $\times$ (8,9,11,14,18,23)), with a circular beam of 2″, as shown in the bottom right corner, are overlaid on the color-scale image of intensity integrated between 35 and 170 km s^{-1}; this range corresponds to the Northern Arm emission. The plus sign indicates the position of the stellar IR source. The circles indicate the three regions for which spectra are shown at the right: (1) a location at which there is emission only from the IRS 8 nebula, (2) a location corresponding to the bow shock, at which there is emission from both the Northern Arm and the IRS 8 nebula, and (3) a location showing line emission only from the Northern Arm. (b) Plot of intensity-weighted velocity of gas in the range associated with the IRS8 nebula (Geballe et al. 2004). The plus sign indicates the position of the stellar IR source. (c) Intensity-weighted velocity for the Northern Arm component, restricted to 35–170 km s^{-1}. For both the upper left and bottom left figures, the color wedge shows the velocity scale between -25 and +100 km s^{-1}. (d)–(f) The spectra (black) on the right correspond to the three positions indicated, and are taken from the high-angular resolution (1.″25) line cube. The spectrum (red) in (f) is taken from the continuum peak (head of the bow shock) as compared with that (black) of region 2 (tail). (g) The spectrum integrated from the region with a size of 6″ $\times$ 5″ (P.A. = 0°) centered at a position ($-1.''2$, $26.''3$) offset from Sgr A*. The vertical bars indicate the peak velocities -17 km s^{-1} and 76 km s^{-1} for the nebula and bow-shock components, respectively.

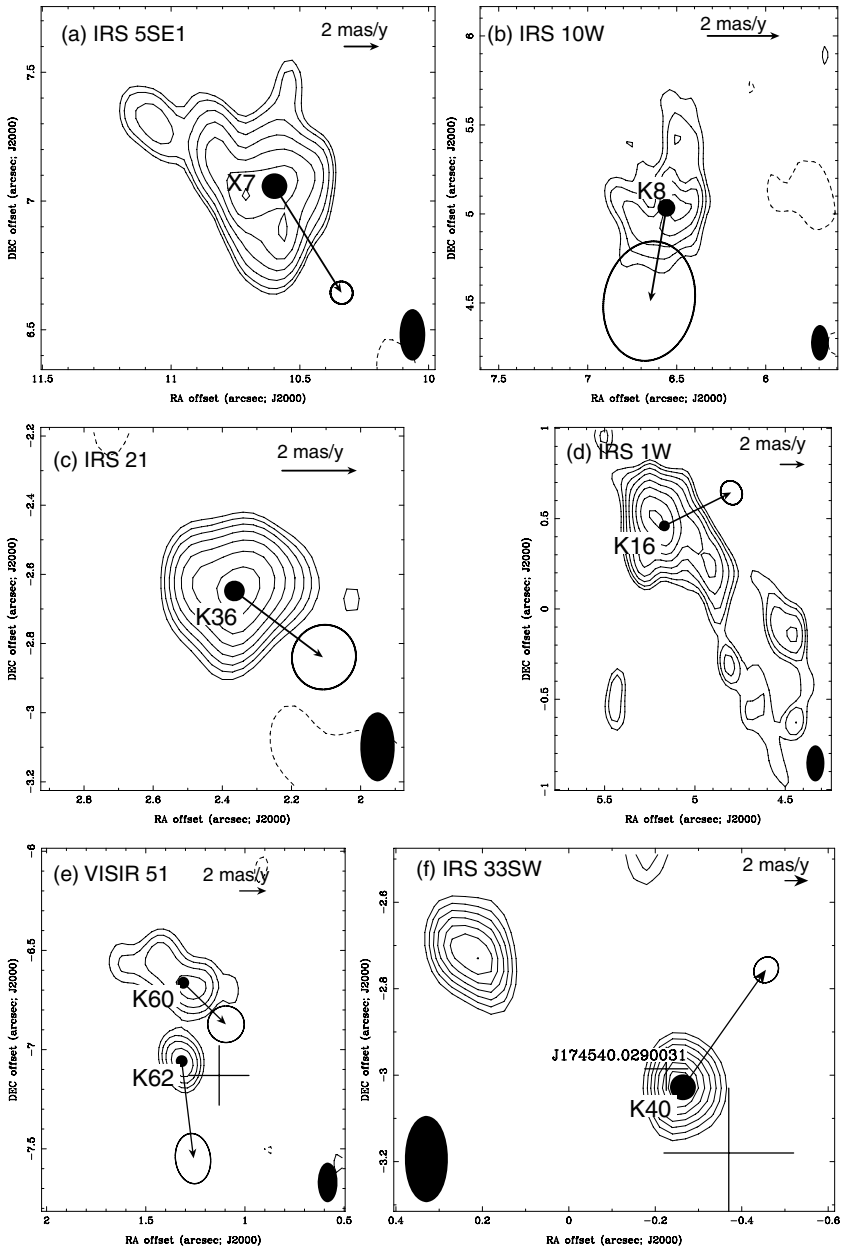

Figure 10. Images of compact radio sources at 1.3 cm in the Northern Arm, made from the 2005K epoch data with the long baseline data only (>100$k\lambda$). The vectors mark the proper motions, with the 2σ uncertainty scaled with the open ellipses for magnitude (the semi-axes along the vectors) and direction (the semi-axes perpendicular to the vectors). The horizontal vectors on the top right of each panel represent a proper motion of 2 mas yr^{-1}. (a) Radio emission (X7) of IRS 5SE1. The contours are 0.035 mJy beam^{-1}×(–3, 3, 4, 6, 9, 13, 18, 24 and 31). (b) Radio source (K8) of IRS 10W with contours of 0.035 mJy beam^{-1}× (–9, 9, 13, 18, 24, and 31). (c) Radio source (K36) of IRS 21 with contours of 0.035 mJy beam^{-1}× (–6, 6, 9, 13, 19, 28, 41, and 59). (d) Radio source (K16) of IRS 1W with contours of 0.035 mJy beam^{-1}× (–6, 6, 8, 11, 15, 21, 28, 37, and 47). (e) Radio emission (K60 and K62) of VISIR 51 with contours of 0.035 mJy beam^{-1}× (–8, 8, 12, 17, and 24). (f) Radio emission (K40) of XJ174540.0290031/IRS 33SW with contours of 0.035 mJy beam^{-1}× (–24, 24, 30, 36, 42, 48, and 54). The FWHM beam shown in all the panels is 0.″2 × 0.″1 (0°).

The Eastern Arm may in fact have several kinematic components. In the H92α line profiles along the portion of the Eastern Arm (see E1–E5 in Figure 5(c)) that Paumard et al. (2004) termed the "Ribbon," one can clearly see the positive-velocity features around +70 to +110 km s^{-1} that correspond to what Paumard et al. (2004) called the "Eastern Bridge," a separate kinematic component. In addition, a weak negative-velocity feature at ∼−100 km s^{-1} is also present (see E7–E9 in Figure 5(c)). Unfortunately, our H92α line data cube does not contain the high positive velocities (>220 km s^{-1}) that are found in the "Tip" feature, which may be related to the Eastern Arm (see Vollmer & Duschl 2000), although the two are quite distinct in the Br-γ spectra of Paumard et al (2004). While Paumard et al. (2004) drew a distinction between the Eastern Arm (their "Ribbon") and the Bar, we find that the quasi-continuity in the position and velocity of the gas in the Eastern Arm (positions E1–E11) and the Bar (positions E13–E17; see Figures 5 and 20) reinforces the possibility that these features can be unified as a single dynamical entity, as was suggested by Liszt (2003). He advanced a circular ring model, which connects the dynamics and placement of the innermost parts of the Eastern Arm with those of the Bar, but does not appear to reproduce the outer structure of the Eastern Arm. Indeed, we show below in Section 5 that the radial velocities and positions are consistent with motion around

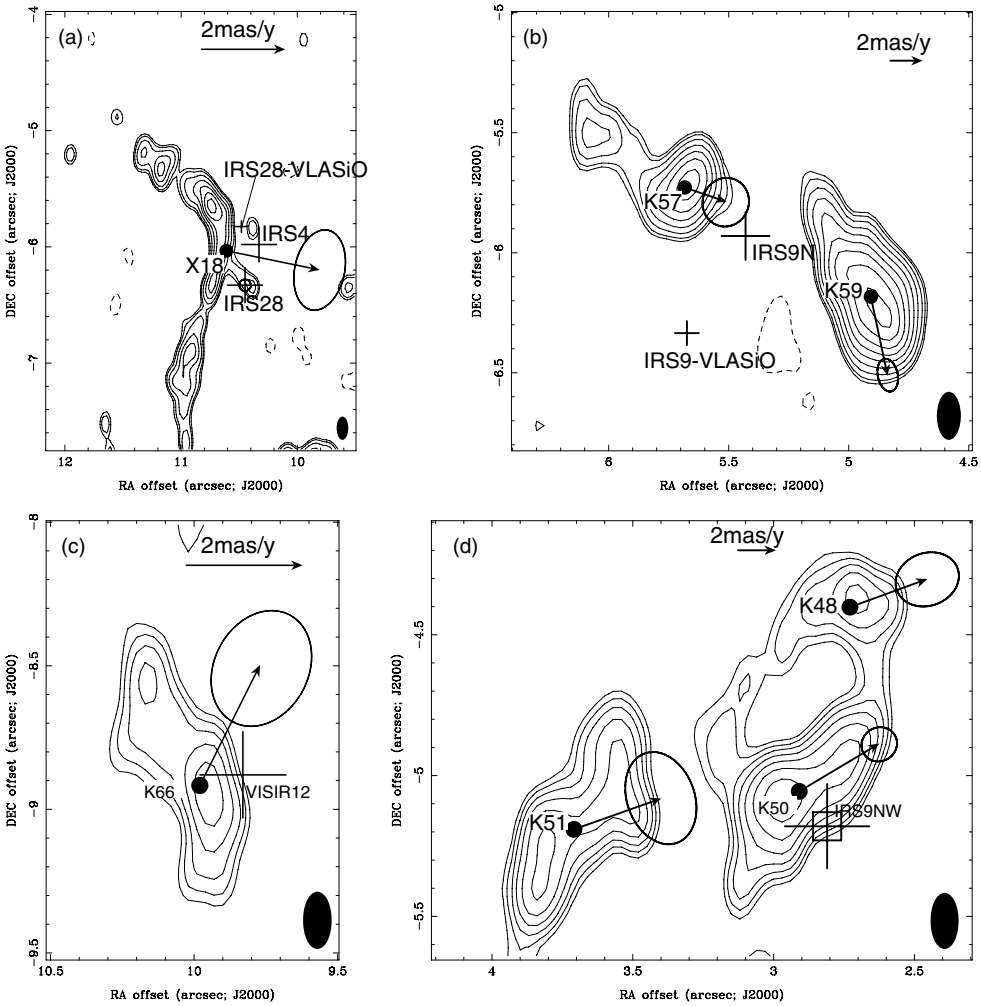

Figure 11. Images of the compact radio continuum sources in the Eastern Arm made from the 2005K epoch data at 1.3 cm with the longer baselines (>100$k\lambda$). (a) Radio emission (X18) of IRS 28/IRS 4/IRS 28-VLASiO. The contours are 0.035 mJy beam^{-1}×(–4, 4, 5, 7, 10, 13, 17, and 22). (b) Radio emission (K57 and K59) of IRS 9N/IRS 9-VLASiO. The contours are 0.035 mJy beam^{-1}× (–12, 4, 5, 7, 10, 14, 19, 25, 32 and 40). (c) Radio emission of VISIR 12 (K66) in contours of 0.035 mJy beam^{-1}×(–8, 8, 12, 17, 23, and 30). (d) Radio emission of IRS 9NW (K50). The contours are 0.035 mJy beam^{-1}× (–6, 6, 8, 11, 15, 21, 28, 36, 45, and 55). The FWHM beam is 0.″2 × 0.″1 (0°). The vectors mark the proper motions of the radio sources with the open ellipses showing the 2σ errors in magnitude (the semi-axes along the vector) and the direction (the semi-axes perpendicular to the vector). The top-right vector on each panel gives the scale for the proper motions (2 mas yr^{-1}).

a single Keplerian orbit. However, the continuity is unclear at around position E12, so the coherence of this feature remains to be demonstrated.

4.4. The Sources in the Western Arc

The radio emission from the Western Arc (Figure 6) is weak and only a few sources are compact and bright enough (S > 1.2 mJy beam^{-1}) for proper motion measurements. Figure 12 shows radio components with measurements of proper motion in the Western Arc. A compact radio component, X6, in the Northern part of the Western Arc shows a double structure (Figure 12(a)). It shows a northeastward motion with an implied transverse velocity of $V_t = 299 \pm 36$ km s^{-1} (P.A.= 66° ± 12°), and the radial velocity from the H92α line is $V_{LSR} = 31 \pm 11$ km s^{-1} at this location. Somewhat to the east of the Western Arc, the compact radio component X24 is identified with the IR star MP-9.0-14.4 (Figure 12(b)). The proper motion measurements suggest that X24 moves southwestward with $V_t = 244 \pm 43$ km s^{-1} (P.A.= −147° ± 9°) and $V_{LSR} = -18 \pm 8$ km s^{-1}. In the Western Arc (Figure 12(c)), the filament X23 shows a northwestward motion with $V_t = 537 \pm 74$ km s^{-1} (P.A. = −25° ± 6°) and $V_{LSR} = -44 \pm 4$ km s^{-1}. Located 5″ NE to X23, X21 shows nearly westward motion with $V_t = 187 \pm 44$ km s^{-1} (P.A.= −72° ± 26°). The H92α line of X21 shows a double profile with peaks at $V_{LSR} = -51 \pm 5$ km s^{-1} and -110 ± 7 km s^{-1}. The weaker component, X19, shows northeastward motion with $V_t = 244 \pm 63$ km s^{-1} (P.A.= 64° ± 23°) and $V_{LSR} = -30 \pm 4$ km s^{-1}. We note that the proper motions of the three components (X19, X21, and X23) appear to be inconsistent with each other, which could result from a substantial contribution of non-orbital motions. If non-orbital motions are random, a vector average could help reduce the effect of non-orbital motion in the orbital fitting program discussed in Section 5. The mean proper motion in this region obtained by vector averaging the three components is $\overline{\mu}_\alpha = -3.61 \pm 0.74$ mas yr^{-1} and $\overline{\mu}_\delta = 2.52 \pm 0.49$ mas yr^{-1}, corresponding to $\overline{V}_t = 167 \pm 25$ km s^{-1} (P.A. = −55° ± 13°) northwestward.

*4.5. The Sources Near Sgr A**

Figure 13 shows the radio images at 1.3 cm (color for the epoch 2005K) and 3.6 cm (contours for the epoch 2002X) along

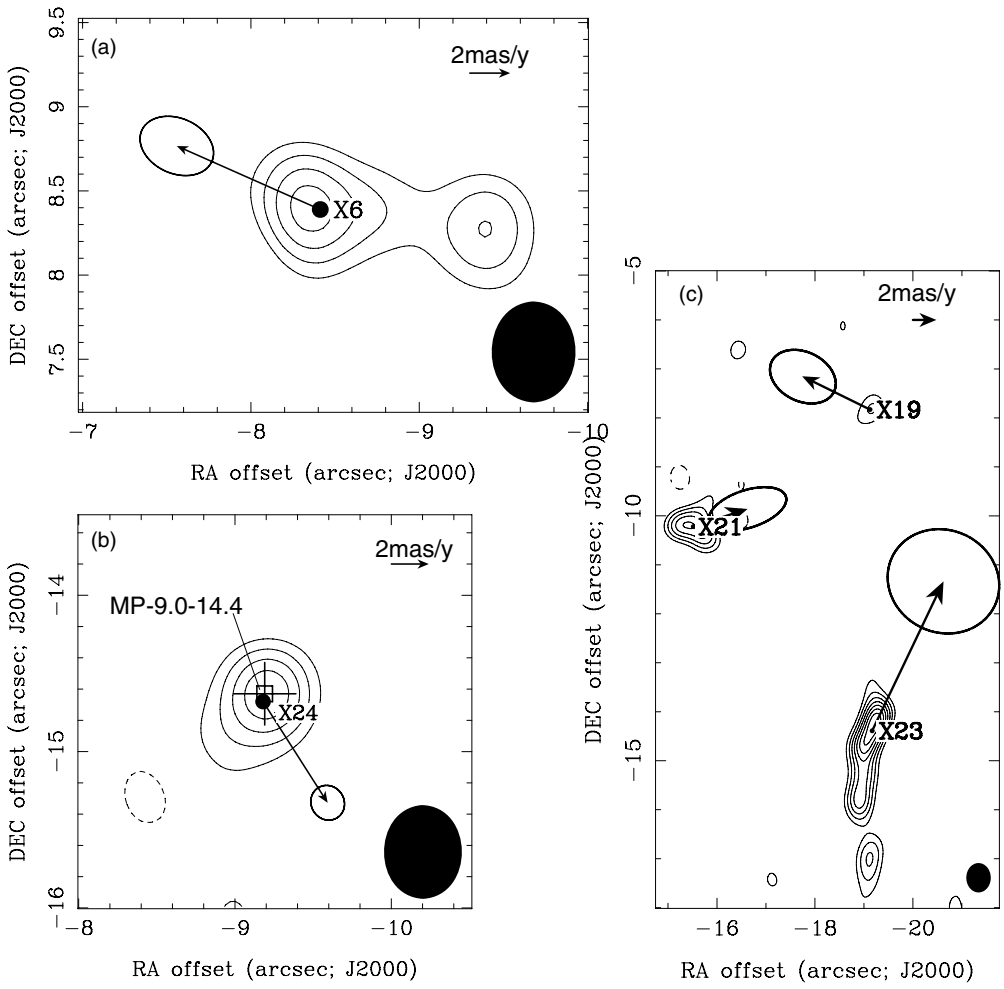

Figure 12. Images of the compact radio continuum sources at 3.6 cm in the Western Arc made from the 2002X epoch data with the longer baselines (>100$k\lambda$). (a) The double radio emission (X6). The contours are 0.4 mJy beam^{-1}×(–2, 2, 3, 4, and 5). (b) The radio emission (X24) of MP-09-14.4. The contours are 0.4 mJy beam^{-1}×(–2, 2, 3, 4, and 5). (c) Radio emission (X19, X21, X23) in contours of 0.4 mJy beam^{-1}×(–2, 2, 3, 4, 5, 6, 7, and 8). The FWHM beam is 0.″6 × 0.″5 (P.A. = 0°), shown as a filled ellipse at bottom right. The vectors show the proper motions of the radio sources, with the open ellipses showing the 2σ errors in magnitude (the semi-axes along the vector) and direction (the semi-axes perpendicular to the vector).

with the positions of the IR stars in the IRS 16 region. The most prominent feature in both the 1.3 and 3.6 cm images is the linear feature (∼4″ in length, <0.″5 in width), located at the NW edge of the Northern Arm. In the middle of the linear feature, there is an elongated radio component, K20. The radio source K20 may be associated with the He I star (He I–N2), which shows a P-Cygni He I profile (Paumard et al. 2001). The radial velocity of the star determined from IR line observations, -97^{-64}_{+56} km s^{-1}, is similar to that of the Northern Arm gas in the same direction, as determined from the H92α line. However, this coincidence may just be fortuitous. On the other hand, K20 appears to be the compressed, ionized edge of the Northern Arm, which was also observed clearly at 3.8 μm with the VLT (Mužić et al. 2007). This compression plausibly results from the collective winds and radiation pressure from all of the high mass stars in the IRS 16 cluster.

In addition, we searched the literature and only found that MP+2.37−0.29 (Genzel et al. 2000) is close to He I–N2, with proper motion measurement. The magnitude of the star velocity agrees well with that of K20 but the P.A. of the transverse velocity between the two objects differs by more than 100°. K20 shows a southwestward proper motion of $V_t = 354 \pm 19$ km s^{-1} (P.A. = $-136° \pm 4°$), which is consistent with this compressional front being caused by the IRS 16 stars. Two Gaussian components were fitted to the broad spectrum of the H92α line at K20, the dominant one being at $V_{LSR} = -41 \pm 11$ km s^{-1} with $\Delta V_{FWHM} = 137 \pm 37$ km s^{-1}. The total velocity is then $V = 356 \pm 20$ km s^{-1}. Considering the fact that the gas in the Northern Arm stream is located behind Sgr A* based on the LSQ fitting and numerical calculations in Section 5.5, the velocity vector of K20 suggests that the source moves toward its periapse in an orbit that carries it around Sgr A*. If the proper motion of the linear feature indicates the track of the gas motion governed by the gravity of the SMBH, we would expect the velocity of K20 to increase as it approaches Sgr A*. A comparison between its motion and what the dynamical models (Section 5) predict for the transverse velocity would be helpful in understanding the accretion process occurring in the immediate vicinity around Sgr A*.

4.6. Mini-cavity and IRS 13

Figure 14(a) shows the locations of a dozen IR stars in the mini-cavity region, including the IRS 13 and IRS 2 complexes to the West and the IRS 33 complex at the Eastern edge of the cavity. The proper motions of the compact continuum components are shown (Figure 14(b)), suggesting that the bulk motion of the ionized gas in this region is toward the West. The source ε (Yusef-Zadeh & Morris 1991; K22),

the closest component to Sgr A* (offset 1.″6), has a proper motion of $\mu_\alpha = -8.8 \pm 0.5$ mas yr^{-1} and $\mu_\delta = -1.4 \pm 1.5$ mas yr^{-1} or $V_t = 338 \pm 21$ km s^{-1} (P.A. = $-99^\circ \pm 61^\circ$) to the SW, almost directly away from Sgr A*. We note that this is consistent with the model of Wardle & Yusef-Zadeh (1992), who postulated that source ε has resulted from the confluence of gravitationally focused winds from the IRS 16 stars.

The mean proper motion of the components K25, K28, K33, K40, and K45 in the IRS 33 region (NE rim of the "mini-cavity") is $\overline{\mu}_\alpha = -9.3 \pm 0.2$ mas yr^{-1} and $\overline{\mu}_\delta = 1.4 \pm 0.3$ mas yr^{-1} ($\overline{V}_t = 355 \pm 8$ km s^{-1}, P.A.= $-81^\circ \pm 12^\circ$), while for components K32 (source ζ), K41, and K42 (source η; Yusef-Zadeh et al. 1990) in the middle of the "mini-cavity," $\overline{\mu}_\alpha = -5.5 \pm 0.2$ mas yr^{-1} and $\overline{\mu}_\delta = 1.7 \pm 0.5$ mas yr^{-1} ($\overline{V}_t = 218 \pm 9$ km s^{-1}, P.A. = $-73^\circ \pm 16^\circ$). The components K47, K49, K53, and K54 around the SW rim show $\overline{\mu}_\alpha = -5.1 \pm 0.2$ mas yr^{-1} and $\overline{\mu}_\delta = -1.2 \pm 0.4$ mas yr^{-1} ($\overline{V}_t = 199 \pm 8$ km s^{-1}, P.A. = $-103^\circ \pm 19^\circ$). The magnitude of the transverse velocity determined from proper motion measurements appears to be comparable to that of the radial velocity observed from the H92α line.

The most surprising region is the IRS 13 complex (Figure 15), with proper motion vectors pointing in many directions, suggesting that the local stellar winds might be playing a significant role in the motion of the ionized gas (Zhao & Goss 1998; Mužić et al. 2008). However, averaging over the proper motion vectors from the H II components (K21, K23, K24, K26, K27, K29, K31, and K35) in IRS 13, the resultant vector is to the NW, that is, $\overline{\mu}_\alpha = -2.91 \pm 0.04$ mas yr^{-1} and $\overline{\mu}_\delta = 2.50 \pm 0.07$ mas yr^{-1}, corresponding to $V_t = 145 \pm 2$ km s^{-1} (P.A. = $-49^\circ \pm 1^\circ$).

On the other hand, the observations of the H92α line show that in the "Bar" region, a bright emission feature south of Sgr A* (Ekers et al. 1983), there are two distinct velocity components, one associated with the Northern Arm and the other related to the ionized stream in the Eastern Arm (Roberts & Goss 1993). These components are also shown in the Br-γ line observations (Paumard et al. 2004) although the authors did not regard the bar emission as part of Eastern Arm. Figure 16 shows the spectra at the H II components in the "mini-cavity" region covering the velocity range from -415 to 200 km s^{-1}. Around the NE rim, the positive velocity associated with the Eastern Arm stream is prominent while the negative-velocity component associated with the Northern Arm stream is weak with broad-line profile ($\Delta V_{\rm FWHM} > 100$ km s^{-1}). In the mini-cavity, the spectra close to Sgr A* are dominated by components with positive radial velocity. For example, the source ε (K22) has a broad component at $V_{\rm LSR} = 37 \pm 7$ km s^{-1} with $\Delta V_{\rm FWHM} = 63 \pm 16$ km s^{-1} and a narrower ($\Delta V_{\rm FWHM} = 22 \pm 15$ km s^{-1}) feature at a high positive velocity ($V_{\rm LSR} = 165 \pm 5$ km s^{-1}). Of course, possible lines at $V_{\rm LSR} > 200$ km s^{-1} may have been missed due to the limited velocity coverage. The negative-velocity component at -275 km s^{-1} becomes strong about 5″ to the SW of Sgr A* and peaks at the Southern rim (K47) of the mini-cavity. Along the Western rim, the negative-velocity gas shows a trend similar to that in the mini-cavity, that is, it appears to be strong, broad, and localized at the SW rim (K43) and it becomes weak as it moves closer to Sgr A*. In comparison with the negative-velocity component, the positive-velocity ($\sim$+50 km s^{-1}) component becomes stronger and broader as it gets closer to Sgr A*. The H92α line observations also suggest that the mini-cavity was created by strong interactions between various flows. Morris & Yusef-Zadeh (1987) proposed that the mini-cavity might be due to the winds from massive stars in this region. Other interactions,

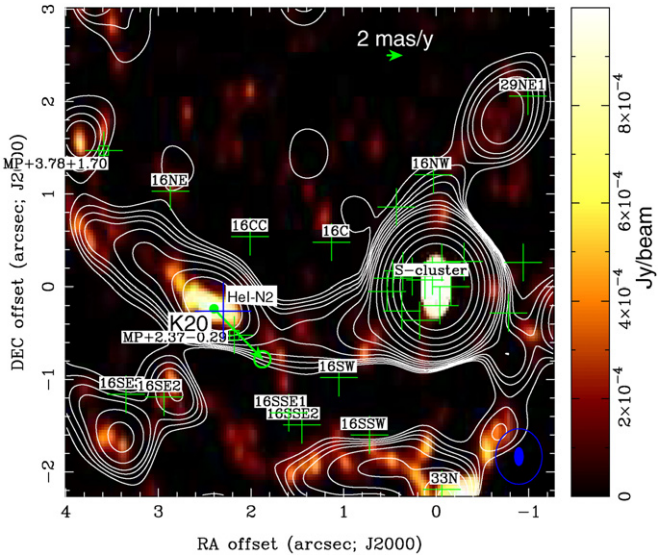

Figure 13. Radio image of the compact components in the region of IRS 16 constructed from the epoch 2005K data at 1.3 cm (color) and epoch 2002X data at 3.6 cm (contours) using only the longer baseline visibilities (>100$k\lambda$). The FWHM beams are shown at bottom right: the filled ellipse (0.″2 × 0.″1, 0°) and the open ellipse (0.″6 × 0.″5, 0°) for images at 1.3 and 3.6 cm, respectively. The contours are 0.25 mJy beam^{-1} ×(1, 2, 3, 4, 6, 9, 13, 18, 36, 72, 144, 288, 576). The plus signs show the positions of the He I stars (Paumard et al. 2001). The plus-empty-squares are the positions of IR stars from Genzel et al. (2000). The stars in the IRS 16 and S-cluster are marked with small plus signs (Paumard et al. 2006). The vector marks the proper motion of the source K20 (coincident with He I–N2, marked with big plus) along with the open ellipse showing the 2σ uncertainty in magnitude (the semi-axis along the vector) and direction (the semi-axis perpendicular to the vector). The horizontal vector at top right shows a proper motion 2 mas yr^{-1}.

such as the interaction between the Eastern and Northern Arm streams or the interactions between outflows from Sgr A* and the streams, might also cause high temperature and therefore a depression in the radio free–free emission. The high LTE temperature (T_e^*) in the Bar reported by Roberts & Goss (1993) might be owing to such an interaction.

4.7. The IRS 6 and and IRS 34 Region

Figure 17 shows the radio sources in the IRS 6/IRS 34 region, which is located 6″NW of Sgr A* (Figure 6). In Figure 18, the H92α line shows a noticeable gradient in radial velocity from $V_{\rm LSR} = -102 \pm 10$ km s^{-1} at (K19) to $V_{\rm LSR} = -184 \pm 5$ km s^{-1} at (K11). This velocity gradient was also detected by Roberts et al. (1996). The velocity gradient observed in the H92α line agrees well with that observed in the Br-γ line (see Figure A.2(b) of Paumard et al. 2004). The H92α line spectrum at K19 (Figure 3(a)) contains at least three Gaussian components. Averaging the vectors from the H II components (K10, K11, K13, K14, K17, and K19) in the IRS 6 region, we derive the mean proper motion of $\overline{\mu}_\alpha = -3.4 \pm 0.2$ and $\overline{\mu}_\delta = 1.4 \pm 0.2$ mas yr^{-1}, suggesting a bulk motion toward the NW ($V_t = 139 \pm 8$ km s^{-1}, PA= $-68^\circ \pm 8^\circ$).

High velocity of the Bullet (X12) was reported early based on proper motion measurements at 2 and 1.3 cm (Yusef-Zadeh et al. 1998; Zhao & Goss 1998). At 1.3 cm, the structure is resolved to at least three knots with varying peak intensities in time, which results in large uncertainties in proper motion measurements. Instead, we use the low-resolution data at 3.6 cm to determine the proper motion of the centroid position of the source. We confirm that the source moves NW but the magnitude of the transverse velocity is reduced by a factor of $\sim$3: $V_t = 319 \pm 37$ km s^{-1}

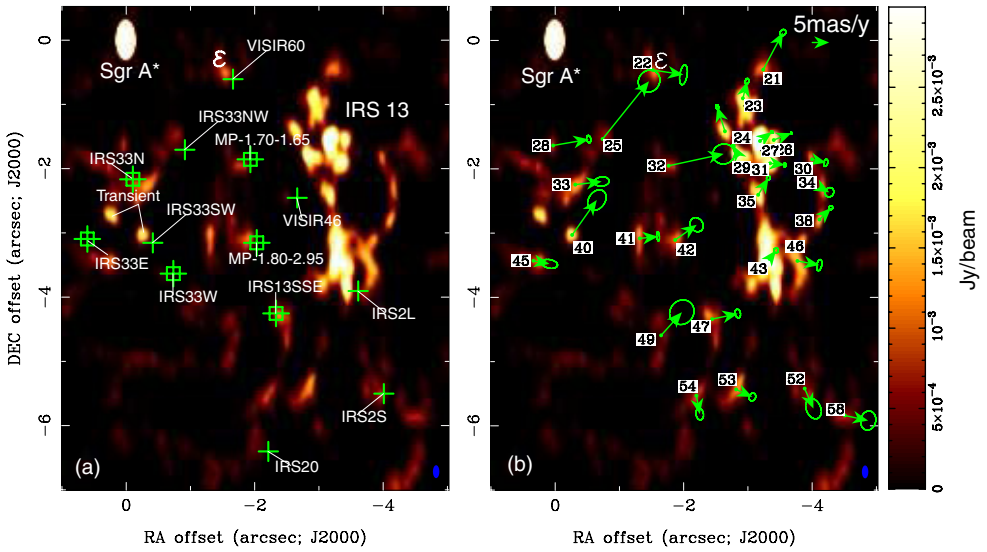

Figure 14. Mini-cavity (Yusef-Zadeh et al. 1989) observed at 1.3 cm. (a) Finding a chart for IR sources: plus symbols from Viehmann et al. (2005) and plus-open-square symbols from Genzel et al. (2000) and Paumard et al. (2006). (b) Proper motion vectors with 2σ errors. The vector (5 mas yr^{-1}) at top right scales the proper motions.

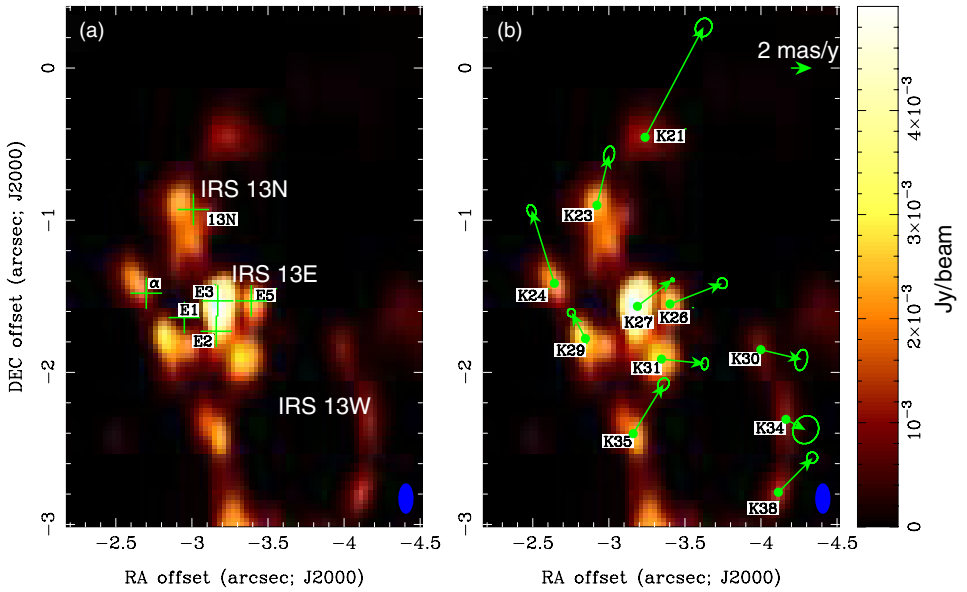

Figure 15. IRS 13 observed at 1.3 cm. (a) Finding chart. The plus signs mark the IR positions of E1, E2, E3, E5, α, and the averaged 13N components from Mužić et al. (2008). (b) Proper motion vectors with 2σ errors. The vector at top right scales the proper motions.

(P.A. = $-53^\circ \pm 12^\circ$). The revised transverse velocity appears to be consistent with the velocity of the ionized flow in the Eastern Arm at this location. However the radial velocities of the two spectral features, $V_{\rm LSR} = -25 \pm 9$ km s^{-1} and $V_{\rm LSR} = 70 \pm 13$ km s^{-1} (Figure 3(c)), deviates significantly from the value at this location predicted from the Keplerian model.

4.8. The Overall Three-dimensional Velocity Field

We imaged the peak radial velocity values derived from the H92α line in the central $80'' \times 80''$ (Figure 18). The mean transverse velocities along the x and y axes of the radio knots in the three ionized arms were determined by averaging the proper motions of several individual radio knots given in Table 2. The mean values of the transverse velocities with respect to Sgr A* ($\overline{V}_x$, $\overline{V}_y$), the mean radial velocity with respect to the LSR ($\overline{V}_{\rm LSR}$), and the mean position offsets from Sgr A* ($\overline{\Delta\alpha}$, $\overline{\Delta\delta}$) were derived and are summarized in Table 4. Column 1 lists the name of the region in which the three-dimensional velocities were determined. The radio IDs in Column 2 indicate the radio knots that were included in the averaging. Column 3 gives the IRS names of the sources in the corresponding regions. Figure 18 shows the images of the vectors of the transverse velocities superimposed on the image of peak radial velocities in the ionized arms based on the VLA observations of the H92α line. The proper motion vectors determined from the VLA observations suggest that all three streams appear to move around Sgr A* in the sense of counterclockwise rotation, as viewed from the Earth.

5. DYNAMIC MODELS FOR THE IONIZED STREAMS

5.1. Three Bundles of Keplerian Orbits

In the case of elliptical motion, adopting the distance (D = 8 kpc), there are six orbital parameters (a, e, Ω, ω, i, $M_{\rm dyn}$) to completely describe an orbit projected onto the plane of the sky.

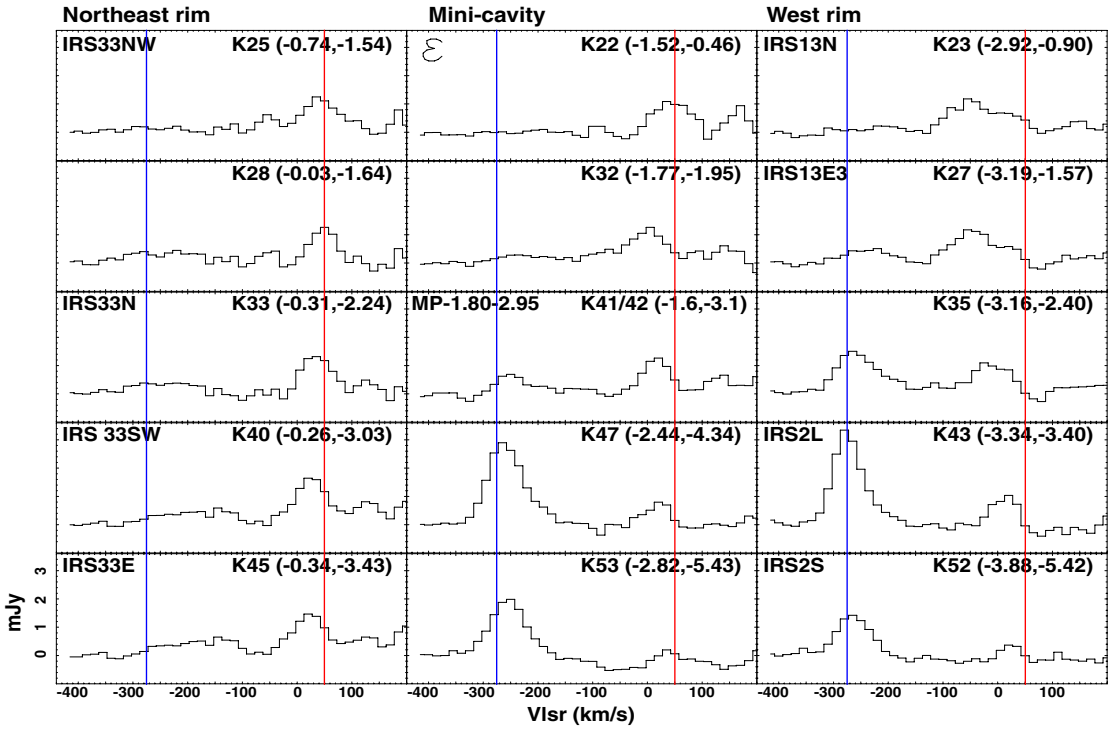

Figure 16. H92α line spectra in the "mini-cavity" and the NE and west rim, taken from the line image with $\theta_{\rm FWHM} = 1\farcs25$. The source ID and the position offsets from Sgr A* are given at top right in each panel. The commonly used names are at upper left. The vertical blue and red lines indicate $V_{\rm LSR} = -275$ km s^{-1} and $V_{\rm LSR} = +50$ km s^{-1}, respectively.

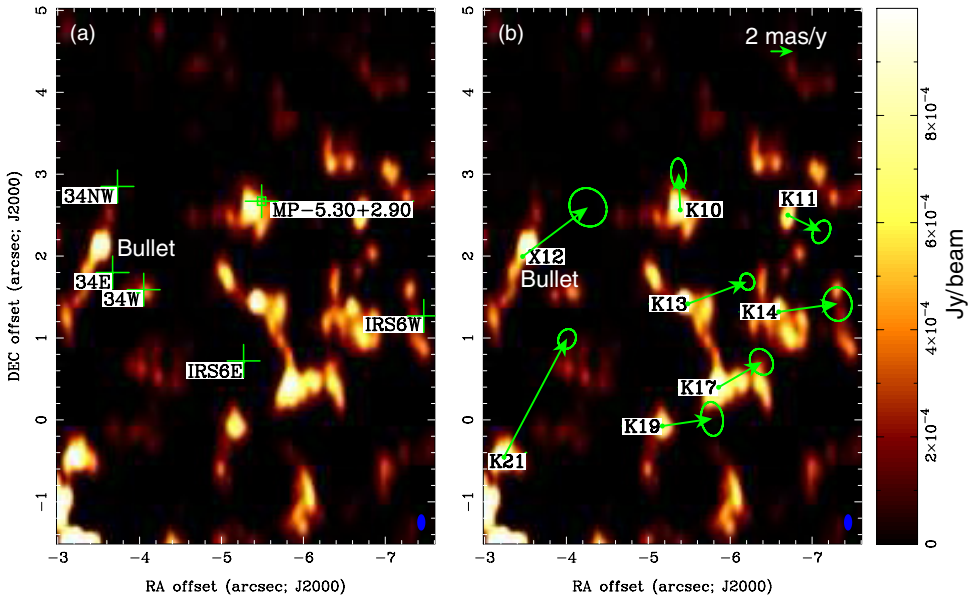

Figure 17. IRS 6/34 region observed at 1.3 cm. (a) Finding chart. The IR sources are marked with plus signs (Paumard et al. 2006) and plus-open-square (Genzel et al. 2000). (b) Proper motion vectors with 2σ errors. The vector (2 mas yr^{-1}) at top right scales proper motions.

Here, a is the size of the semimajor, e is eccentricity, $M_{\rm dyn}$ is the dynamical mass, Ω is the longitude of the line of nodes, ω is the angle of periapsis with respect to the line of nodes, and i is the inclination angle. Based on the assumptions that the positions determined in Section 3, which follow the locus of the stream in each of the arms, are located along a single, Keplerian orbit and that the central mass is fixed at the location of Sgr A*, the orbital parameters (a, e, Ω, ω, i) for the orbital geometry can be determined with LSQ fitting to those positions. The dynamical mass ($M_{\rm dyn}$), on the other hand, can be subsequently determined by fitting the radial velocities in each of the streams. The detailed procedure for determining the orbital parameters is developed and described in the Appendices.

We apply this technique to Sgr A West. Figure 19 shows the fits (solid ellipses) to the observed loci (dots) for each of the three streams. For the loci along each stream, four sets of solutions for the orbital parameters (a, e, Ω, ω, i) can be derived from the LSQ fitting of the quadratic Equation (A1). The first two geometrical parameters (a, e) are the same for all the solutions. The four combinations of the three angular parameters (Ω, ω, i) correspond to the two mirror images about the sky plane, and in each of these, the direction of flow can

Table 4
Three-dimensional Velocities in Sgr A West

Region	IDs of Radio Knots	IR Sources	$\overline{\Delta\alpha}$[a] (arcsec)	$\overline{\Delta\delta}$[a] (arcsec)	$\overline{V_x}$[b] (km s^{-1})	$\overline{V_y}$[b] (km s^{-1})	$\overline{V_{\rm LSR}}$[b] (km s^{-1})
			Northern Arm				
Na	K1	IRS8	1.40 ± 0.01	29.25 ± 0.01	69 ± 14	−42 ± 19	−12 ± 6
							93 ± 28
Nb	K8, X7	IRS5, IRS10	10.22 ± 0.01	5.03 ± 0.01	−54 ± 20	−168 ± 20	67 ± 2
Nc	K16, K20	IRS1, IRS16	3.78 ± 0.01	−0.08 ± 0.01	−218 ± 13	−110 ± 13	15 ± 1
Nd	K36	IRS21	2.37 ± 0.01	−2.65 ± 0.01	−91 ± 15	−67 ± 17	−92 ± 4
Ne	K43, K46, K52	IRS2	−3.43 ± 0.01	−3.61 ± 0.01	−107 ± 6	42 ± 15	−274 ± 1
			Eastern Arm				
Ea	K66, X18	IRS4, IRS28	10.12 ± 0.01	−8.50 ± 0.01	−67 ± 8	24 ± 14	158 ± 3
Eb	K57, K59	IRS9	5.17 ± 0.01	−5.96 ± 0.01	−48 ± 10	−130 ± 16	139 ± 3
Ec	K48, K50, K51	IRS9NW	3.05 ± 0.01	−4.92 ± 0.01	−161 ± 14	81 ± 13	165 ± 13
			Western Arc				
Wa	X6	...	−8.41 ± 0.01	8.37 ± 0.01	193 ± 38	121 ± 23	31 ± 11
Wb	X19, X21, X23	...	−18.00 ± 0.01	−11.75 ± 0.01	−137 ± 28	96 ± 18	−67 ± 5
Wc	X25	...	−15.37 ± 0.01	−3.52 ± 0.01	−64 ± 15	140 ± 19	−90 ± 4
			Bar				
Ba	K25, K33, K40	IRS33	−0.27 ± 0.01	−2.81 ± 0.01	−296 ± 14	124 ± 22	−85 ± 6
							34 ± 3
							161 ± 4
Bb	K21, K23, K24, K26 K27, K29, K31, K35	IRS13	−3.18 ± 0.01	−1.58 ± 0.01	−110 ± 2	95 ± 3	−37 ± 2
							−247 ± 4
Bc	K10, K11, K13, K14, K17, K19	IRS6, IRS34	−6.01 ± 0.01	1.33 ± 0.01	−128 ± 6	51 ± 9	−180 ± 4

Notes.
[a] The mean position offsets derived by averaging the position offsets of the radio knots listed in Column 2 of this table.
[b] The mean velocities derived by averaging the velocity components of the radio knots listed in Column 2 of this table.

be clockwise or counterclockwise. The proper motions can be used to decide between clockwise and counterclockwise, and the sign of the radial velocities determines which of the mirror images is correct.

Figure 18 shows the measured vectors of the transverse velocities distributed in each of the three streams, showing that the ionized streams are in counterclockwise rotation around the dynamical center. The remaining degeneracy of the two mirror images can be solved by the radial velocity determined from the H92α line. Thus, we can unambiguously determine the orbital parameters for the three major streams in Sgr A West.

There is no principle dictating that the gas arrayed along any given stream must all be on the same Keplerian orbit. Indeed, gas in a tidally sheared cloud, which may describe these streams, will in general be different orbits, depending on where it was located in the original cloud. However, except under unusual circumstances, such as a radially infalling cloud, the orbits assumed by the different parcels of gas within a shearing cloud will be rather similar, and the ensemble of orbits will be a family of similar orbits. We therefore adopt the simplification of a single orbit in order to characterize the orbit family. The assumptions underlying this procedure are somewhat vindicated by our success in fitting single orbits to the streams.

Table 5 summarizes the LSQ solutions of the orbital parameters for the three streams from the best fits. Both the Northern Arm and Eastern Arm streams appear to be in Keplerian motion on high-eccentricity elliptical orbits of $e = 0.83 \pm 0.10$ and 0.82 ± 0.05, respectively. Our best fit for the Western Arc stream indicates that it is in a nearly circular orbit ($e = 0.20 \pm 0.15$), consistent with what has previously been suggested (Roberts & Goss 1993; Lacy et al. 1991). Constrained by proper motion measurements which show that all three streams rotate in a counterclockwise sense around Sgr A*, the inclination angles must be greater than 90°. From the best-fitted solutions above, we can unambiguously determine the inclination angles to be 139 °± 10°, 122 °± 5°, and 117 °± 3° for the Northern Arm, Eastern Arm, and Western Arc, respectively.

5.2. Dynamical Mass in Sgr A West

The above analysis does not yield information on the mass. In order to determine the dynamical mass, velocity information is required. If the radial velocity of Sgr A* with respect to the LSR, the transverse velocity of Sgr A* with respect to that of the dynamical center, and the position offsets of Sgr A* from the dynamical center can be neglected, then $V_z = V_{\rm LSR}$ and the location of Sgr A* defines the dynamic center. For a given total velocity $V = \sqrt{V_x^2 + V_y^2 + V_z^2}$ at position (x, y, z), the dynamical equation relating V to the mass ($M_{\rm dyn}$) is

$$V = M_{\rm dyn}^{1/2} \left(\frac{2}{r} - \frac{1}{a} \right)^{1/2}, \quad (1)$$

where r is the radial distance from the dynamical center, which can be expressed as a function of the projected coordinates (x, y) in Equation (B2).

In principle, the dynamical mass in Sgr A West can be derived by fitting the total velocity to Equation (1). Since only a few measurements of proper motion in the outer region of Sgr A West are available, the fit of the measured total velocities leaves a sizeable uncertainty in the determination of the dynamical mass. On the other hand, our radial velocity measurements from each of the three orbits cover a large fraction of the complete orbits of each flow, so we can use the radial velocities to constrain the

Table 5
Orbital Parameters of the Three Streams in Sgr A West

Orbital Parameters	(Units)	Northern Arm	Eastern Arm	Western Arc
Distance ($\int$D)	(kpc)	8	8	8
Mass ($M_{\rm dyn}$)	($10^6\ M_\odot$)	4.2^{+6}_{-3}	4.2^{+6}_{-3}	4.2^{+6}_{-3}
Eccentricity (e)		0.83 ± 0.10	0.82 ± 0.05	0.20 ± 0.15
Semimajor axis ($a \pm \Delta a$)	(kAU)	205 ± 91	289 ± 140	236 ± 12
	(pc)	0.99 ± 0.44	1.40 ± 0.68	1.11 ± 0.06
Longitude of the ascending node ($\Omega \pm \Delta\Omega$)[a]	(deg)	64 ± 28	−42 ± 11	71 ± 6
Argument of perifocus ($\omega \pm \Delta\omega$)	(deg)	132 ± 40	−280 ± 8	22 ± 48
Inclination ($i \pm \Delta i$)[a]	(deg)	139 ± 10	122 ± 5	117 ± 3
Perifocal distance (q)	(kAU)	34	52	184
	(pc)	0.17	0.25	0.89
Period (T)	(10^3 yr)	45	76	54

Notes.
[a] Following the convention of astrodynamics (Boulet 1991), Ω is the angle between the $+x$-axis (East) and a line from the dynamic center to the point where the object crosses the sky plane from the negative to positive side of the z-axis measured counterclockwise as viewed from the $+z$ direction (pointing away from the Earth). The inclination i is the angle between the $+z$-axis and the angular momentum vector $\boldsymbol{h}$, which is perpendicular to the orbit plane, measured from 0° to 180°. If $i > 90°$, the orbital motion is counterclockwise as viewed from the Earth. If $i < 90°$, the orbital motion is clockwise as viewed from the Earth.

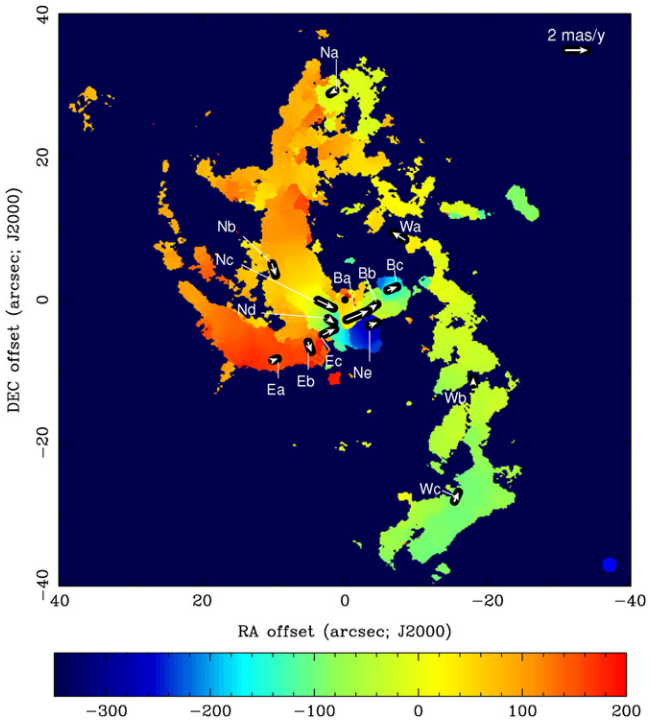

Figure 18. Representation of the measured three-dimensional velocity field in Sgr A West (the central 80 arcsec or 3 pc). The color map shows the radial velocity (V_z) determined by fitting the peak velocity of H92α line spectra observed with the VLA. The color wedge shows the velocity scale from +200 to −350 km s^{-1}, red for redshift and blue for blueshift. The vectors show the mean transverse velocities (V_x, V_y) of the radio components in regions summarized in Table 4. The scaling vector at top right shows 300 km s^{-1} in transverse velocity. The black dot indicates the position of Sgr A*. The x- and y-coordinates are the right ascension and declination offsets from Sgr A*.

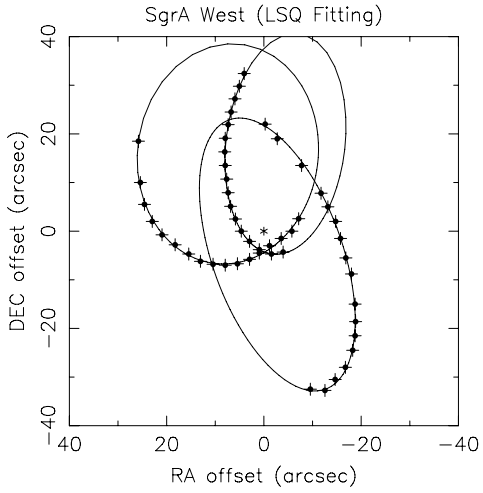

Figure 19. LSQ fitting (solid curves) to position data (dots) along the loci of the three streams observed in the H92α line emission from Sgr A West (the central 80 arcsec or 3 pc). The positions are marked in Figure 5(a). The size of each cross represents the size of the region over which the radial spectra (Figure 5(b)) were integrated. The star indicates the position of Sgr A*. The coordinates are the right ascension and declination offsets from Sgr A*, at the dynamic center.

dynamical mass with Equation (B1). With the best-fit orbital parameters (a, e, Ω, ω, i), we solve Equation (B1) using our orbit models for three values of the central mass, that is $M_{\rm dyn} = (1.2, 4.2, 10) \times 10^6\ M_\odot$, and compare the predicted radial velocities to those measured at each position along the orbits. Figure 20 shows the results of fitting in each of the three streams. In general, the model with a mass of $M_{\rm dyn} = 4.2 \times 10^6\ M_\odot$ fits the data, consistent with the prevailing view that the mass of Sgr A* determined by fitting the orbits of the IR stars (Ghez et al. 2008, 2003, 2005; Schödel et al. 2002) dominates the central dynamics. However, not surprisingly, there are some deviations between the model and data (see Figure 20). The deviations of the radial velocity in the inner region can be attributed to some local nongravitational effects such as winds, MHD flows, magnetic pressure gradients, and possibly interactions between streams. Deviations at larger radii might result from the increasingly important contribution of stars to the enclosed mass as the radius increases, thus causing deviations from pure Keplerian orbits. Of course, many of these apparent deviations could simply result from the failure of the basic assumption in this analysis: that each of the three streams follows a unique Keplerian orbit. In any case, the total dynamical mass in the central 3 pc appears to be $\sim 1 \times 10^7\ M_\odot$.

5.3. Model Calculation and Three-dimensional Location of the Three Streams

The fitted parameters are summarized in Table 5 for the three streams in Sgr A West. Using these parameters, we have modeled these streams as the model of three bundles of Keplerian orbits. In addition to the best-fitted orbital parameters

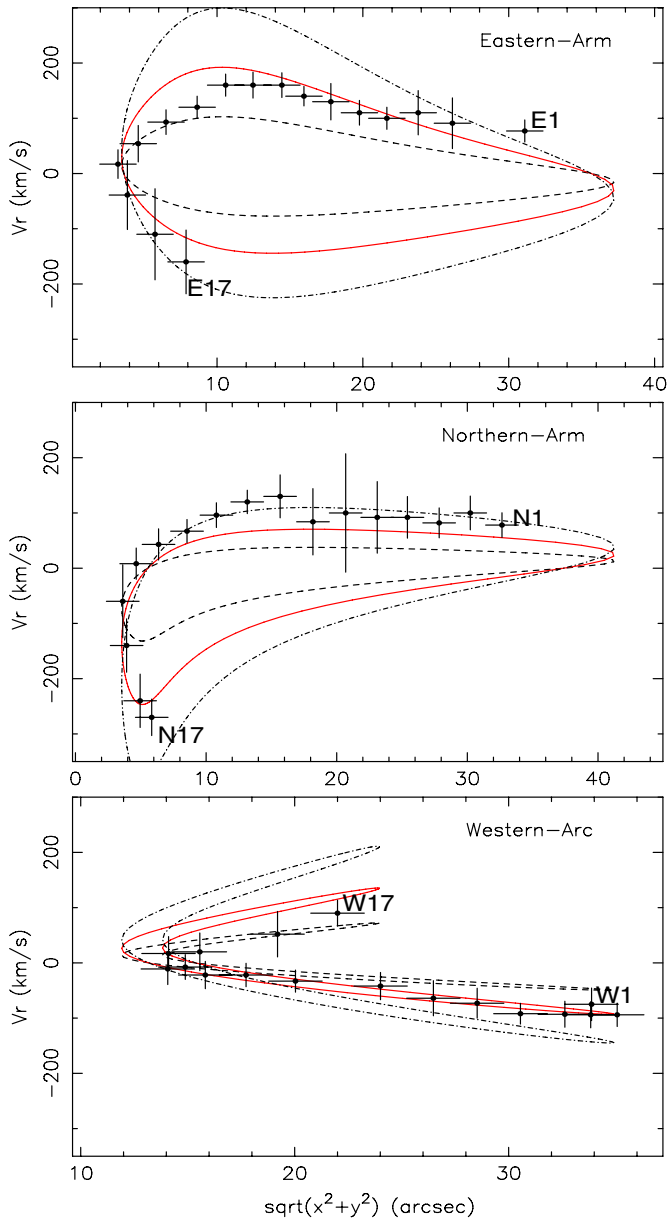

Figure 20. Diagrams of radial velocity (V_z) vs. projected distance ($\sqrt{x^2+y^2}$) with respect to the dynamical center for the three streams associated with the Eastern Arm, Northern Arm, and Western Arc. Dots are the measurements of radial velocities ($V_{\rm LSR}$). The horizontal bars represent the radius of the region from which $V_{\rm LSR}$ was measured. The vertical bars are the FWHM of the velocity component. The solid (red) lines indicate the fits of the model (Equation (7)) with the best-fitted orbital parameters (a, e, Ω, ω, i; Table 5) and a mass of $M_{\rm dyn} = 4.2 \times 10^6\ M_\odot$, the mass of the SMBH, to the data. With the orbital parameters remaining fixed, the dashed lines indicate the fits with a mass of $M_{\rm dyn} = 1.2 \times 10^6\ M_\odot$ while the dash-dot lines correspond to the fits with a mass of $M_{\rm dyn} = 10.2 \times 10^6\ M_\odot$.

(A color version of this figure is available in the online journal.)

(Table 5), we also used the dynamical mass of $M_{\rm dyn} = 4.2 \times 10^6\ M_\odot$ and a dispersion of $\Delta a = \pm 0.25a$ in the semimajor axis to roughly match the width of the orbits in each of the streams. The ranges of the true anomaly 192°−460°, 195°−430°, and 130°−420° were used to calculate the three streams for the Northern Arm, the Eastern Arm, and the Western Arc, respectively.

The comparison between the observed kinematics of Sgr A West and the calculation based on the best-fitted orbital model is shown in Figure 21. The radial velocities (V_z) of the streams are plotted in Figure 21(b). The vectors of the transverse velocity (V_x, V_y) are illustrated in Figure 21(c). The three-dimensional velocity field calculated from our model appears to be in good agreement with the observations. In other words, the three bundles of elliptical orbits along with the orbital parameters (a, e, Ω, ω, i) derived from the LSQ fitting are consistent with the model calculations.

The locations of the three streams along the line of sight are shown in Figure 21(d), suggesting that most of the orbiting ionized gas in the "Bar" region is located behind Sgr A*. The highly inhomogeneous distribution of the ionized gas allows the low-frequency ($\nu \sim 0.3$ GHz) radio emission from Sgr A*, which is subject to strong free–free absorption, to pass through the gap in the ionized streams, as was suggested from the VLA and Giant Metrewave Radio Telescope (GMRT) observations (An et al. 2005).

The total velocity and kinetic energy per unit mass were also calculated and are shown in Figures 21(e) and (f), respectively. The figures show that the specific kinetic energy of both the Northern and Eastern Arms reaches a maximum in the "Bar" region. The high specific kinetic energy density there emphasizes the possibility that the mini-cavity was created by strong shocks resulting from the collision of the two streams.

6. A MAGNETICALLY DETERMINED MORPHOLOGY IN THE NORTHERN ARM?

The dynamical model discussed above is based on a spherical gravitational potential centered on Sgr A*. However, the magnetic field in the Northern Arm might be strong enough to cause observable deviations from the kinematics determined by gravity alone. Polarization measurements at 12.5 μm of thermal dust emission arising in the Northern Arm indicate that the dust grains in this structure are extremely well aligned by a uniform magnetic field oriented along the long axis of the arm (Aitken et al. 1998; Glasse et al. 2003). The uniformity of the field direction is attributed to shear in the direction of the flow (Aitken et al. 1991), which is inevitable, given that the finite breadth of the Northern Arm gives rise to a significant differential gravitational force across the arm. The magnetic field strength estimated from dynamical considerations and from the application of the method of Chandrasekhar & Fermi (1953) is $\gtrsim$2 mG.

Our high-resolution image at 1.3 cm (Figure 22) reveals a suggestive sinuous structure in the Northern Arm that could have a magnetic origin. Although we do not know the line-of-sight structure of this feature, the morphology is consistent with a projected helix having 1.5–2 well defined wavelengths between decl. (J2000) of –29°00′17.″5 and −29°00′22″. To illustrate this, we show model-projected helices in Figure 22 for comparison with the observed feature. The velocity ($V_x = -18$ km s^{-1}, $V_y = -223$ km s^{-1}, $V_z = 70$ km s^{-1}) at this location ($\Delta x = 7''$, $\Delta y = 10''$) is obtained from the orbital model. The tilt (the angle of the velocity vector with respect to the line of sight) of this Northern Arm fragment is $\arccos(Vz/V) \sim 72°$, which is reasonably consistent with the best-fit projection angles of the model helices. A helix is a natural morphology for a twisted magnetic field frozen into a plasma; the twist could result, for example, from torques exerted on the plasma by reconnection between the Arm field and the ambient field at the surface of the Northern Arm. This process is important in the Earth's magnetotail and results from the "draping" of the solar wind field around the Earth's magnetosphere. It is possible that a

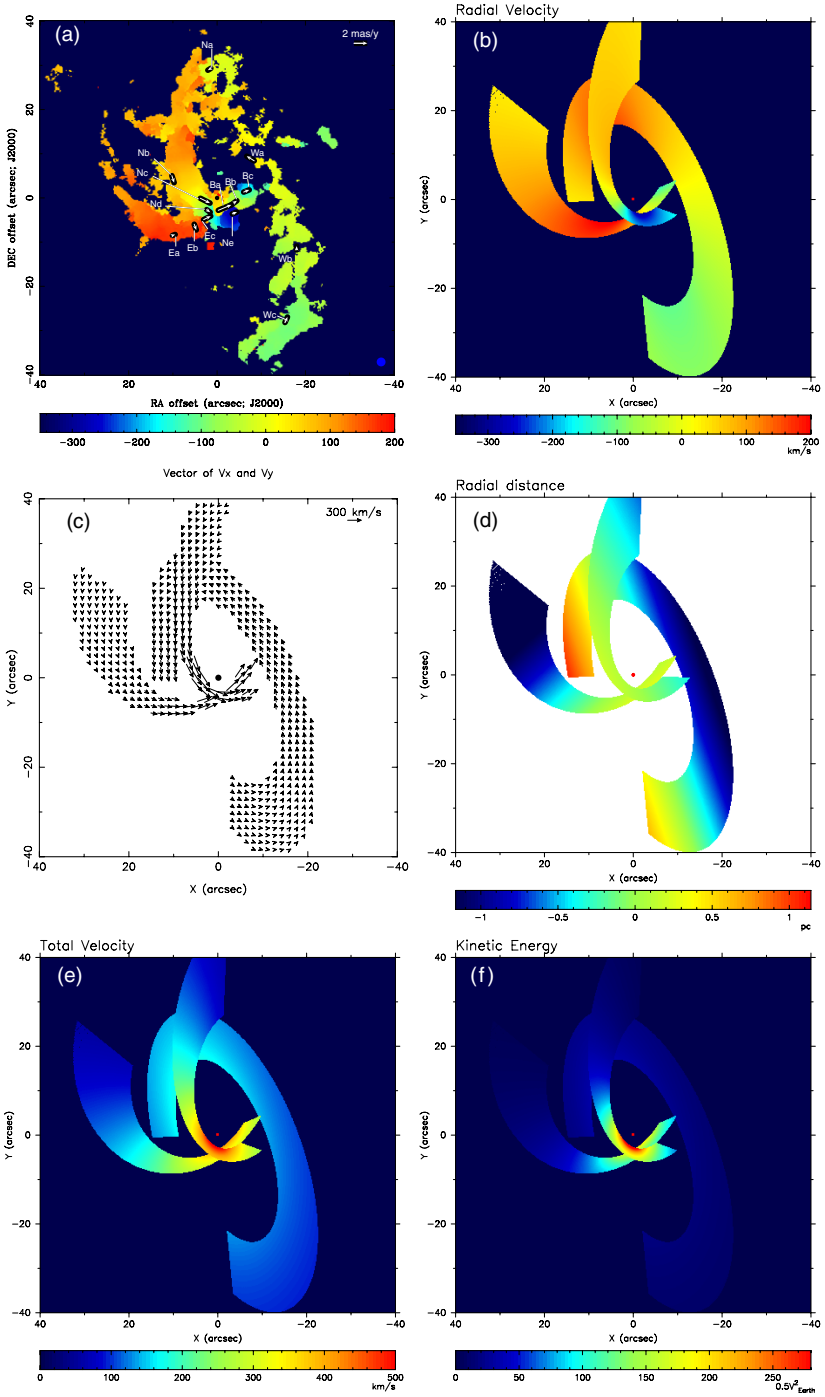

Figure 21. Comparison between the observed kinematics of Sgr A West and the results from the numerical calculation based on the best-fitted orbital model with the parameters summarized in Table 5. (a) The observed radial velocity (color) and transverse velocity determined from proper motions (vectors). The axes are the position offsets from Sgr A*. (b) The radial velocity (V_z) of the three streams in Sgr A West, calculated based on the best-fitted orbital model. For comparison, the illustrated region is at the same scale as the observed one in Figure 21(a). The wedge shows the same scale as that in Figure 21(a). In Figures 21(b)–(f), the dot indicates the position of the dynamical center, coincident with Sgr A*. (c) The calculated transverse velocity (V_x, V_y) of the three streams in Sgr A West. The vector at the top right scales the transverse velocity. (d) The three-dimensional geometry (x, y, z) of the three streams in Sgr A West with respect to Sgr A*, calculated using the fitted orbital model. The color shows the line-of-sight distance (z) from Sgr A* between −1.16 and +1.16 pc. The positive and negative values of z correspond to the regions behind and in front of the dynamical center, respectively. (e) The total velocity $V = \sqrt{V_x^2 + V_y^2 + V_z^2}$ of the three streams in Sgr A West, calculated based on the best-fitted results. The wedge of bottom scales V in units of km s^{-1}. (f) The kinetic energy per unit mass ($\frac{1}{2}V^2$) of the three streams in Sgr A West. The wedge of bottom scales $\frac{1}{2}V^2$ in units of $\frac{1}{2}V_{\rm Earth}^2$, where $V_{\rm Earth} = 29.8$ km s^{-1} is the Earth's mean orbital velocity. In the model images (b)–(f), the X and Y coordinates are the right ascension and declination offsets (arcsec) from the dynamical center, respectively.

similar process occurs in the Northern Arm where the head of the Northern Arm plows through the ambient Galactic center field.

A sinuous morphology in the Northern Arm had previously been noted by Yusef-Zadeh et al. (1989) in a lower-quality 2 cm VLA image (see, e.g., Figure 1 of Yusef-Zadeh et al. 1990) and this structure is evident in Figure 22 of this paper. However, in that case, the wavelength was suggested to be 0.4 pc, much larger than the 0.12 pc wavelength of the feature consid-

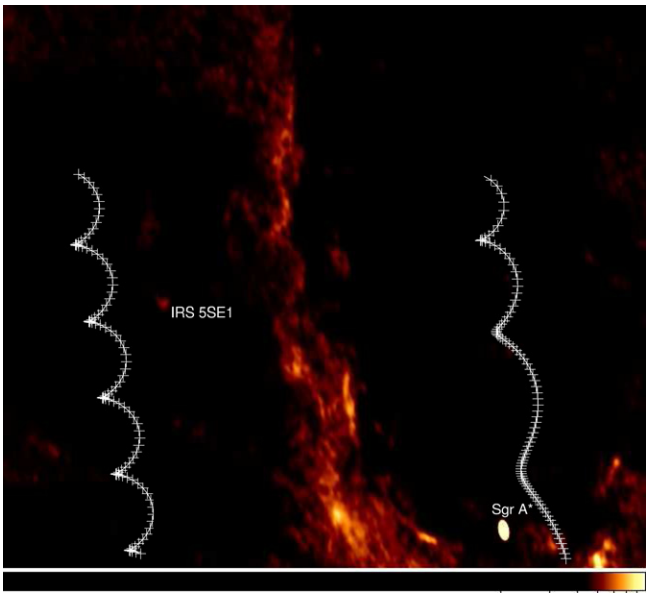

Figure 22. Apparent helical structure of the ionized gas in the Northern Arm observed at 1.3 cm. The bright compact source to the bottom right is Sgr A*. The bow-shock source associated with IRS 5SE1 is also labeled. Also shown are two projected model helices crafted to match the Northern Arm structure. Both are right-handed helices, with the top tilted toward the observer. The model helix at left is tilted by 45° (where 0° corresponds to the helical axis in the plane of the sky) and has a pitch angle of 49°. The helix at the right has a wavelength that increases linearly from top to bottom; it is titled by 50° and the initial pitch angle (at top) is 45°.

ered here. Yusef-Zadeh & Wardle (1993) interpreted this longer wavelength waviness in terms of Rayleigh–Taylor or Kelvin–Helmholtz instabilities caused by winds from the young stars in the IRS 16 cluster. Perhaps there is a homologous structure at multiple scales in the Northern Arm, or perhaps there is an evolution toward increasing wavelength from N to S along the arm as the gas accelerates toward the black hole. In order to investigate this possibility, we considered a model helix in which the wavelength of the helical turns increases southward along the Northern Arm as Sgr A* is approached. This is illustrated by the model helix superimposed on the right side of Figure 22. Although the observed structure becomes more diffuse to the south, there is a good correspondence between this model and the observations.

Observations of the mid-IR polarization vectors and of the velocity field with spatial resolution comparable to that in Figure 22 would provide a test of the hypothesis that a strong magnetic field imposes a helical geometry on the otherwise laminar flow of the Northern Arm. If the pitch angle of $\sim 15^\circ$ reflects the ratio of velocities perpendicular to and along the arm, ~ 0.25, then velocity perturbations as large as 60 km s^{-1} are predicted, using a total flow velocity of 250 km s^{-1} at this location. In radial velocity only, the perturbation may be only a few tens of km s^{-1}. In addition, the mid-IR polarization vectors should everywhere be tangent to the helix.

7. SUMMARY AND CONCLUSION

Using the VLA, we have observed the Galactic center with an angular resolution of 0.″1 at 1.3 cm. Along with the data obtained at previous epochs at 1.3 cm and 3.6 cm, we measured the proper motions of 71 compact H II components in Sgr A West. Using VLA archival data, we constructed an H92α line image cube with angular and velocity resolutions of 1.″25 and 15 km s^{-1}, respectively, covering the velocity range from +200 to -415 km s^{-1}.

With the observed proper motion and radial velocity measurements from the ionized gas, we have investigated the three-dimensional velocity distributions in the central 3 pc. The loci and motions of the three well known ionized streams in Sgr A West can be modeled with Keplerian motions in three bundles of elliptical orbits. We developed a procedure using a least-square fit of the loci of the ionized streams at the Galactic center. The orbital parameters (a, e, Ω, ω, i) were determined confirming that the three ionized streams corresponding to the three radio continuum features (Northern Arm, Eastern Arm, and Western Arc) are confined within the central 3 pc. The dynamics appear to be dominated by the SMBH at Sgr A*, and the total dynamical mass within a radius of 1.5 pc is $\lesssim 1 \times 10^7\ M_\odot$. With the Keplerian model and the fitted orbital parameters, we numerically calculated the kinematics and spatial distribution of the ionized gas. The calculated three-dimensional velocities are in good agreement with the observed velocity distribution, based on the observations of proper motions and radial velocities. This numerical model confirms that three bundles of elliptical orbits with the orbital parameters (a, e, Ω, ω, i) derived from our LSQ fitting and an assumed mass for the SMBH of $4.2 \times 10^6\ M_\odot$ at the dynamical center are a good approach to modeling the dynamics of the ionized gas in the central 3 pc.

With the determined orbital parameters for the ionized streams, our numerical calculations suggest that the Northern and Eastern streams might have collided in the "Bar" region located 5″ SW of Sgr A*. Such a substantial interaction between the two streams could have contributed to the formation of the mini-cavity.

In the IRS 16 region located 2″ E of Sgr A*, the high-resolution observations reveal a linear radio feature (K20). The collective stellar winds and radiation from the IRS 16 cluster are likely responsible for compressing the edge of the Northern Arm at this location and causing it to be particularly bright.

In the IRS 8 region, a radio bow-shock structure is observed, similar to that revealed by IR observations. A shell-like nebula is revealed by the H92α line image showing a narrow feature ($\Delta V_{\rm FWHM} = 52 \pm 17$ km s^{-1}) at $V_{\rm LSR} = -12$ km s^{-1}. The H92α line observations show that the NE part of this nebula physically interacts with the Northern Arm.

Finally, from the high-resolution VLA observations, a helical structure is revealed in the Northern Arm, suggesting that, in addition to the predominantly Keplerian dynamics attributable to the central mass, MHD effects play a role in the production of the detailed structure in the orbiting ionized gas. The predictions from the MHD model are testable with future high-resolution observations of the mid-IR polarization vectors and the velocity field.

The VLA is operated by the National Radio Astronomy Observatory (NRAO). The NRAO is a facility of the National Science Foundation operated under cooperative agreement by Associated Universities, Inc. M.R.M. has been partially supported in this work by NSF grant AST-0406816 to UCLA. T.A. has been supported by the NSFC (10503008). We are grateful to Harvey Liszt for informative and helpful comments.

APPENDIX A

LSQ FIT OF AN ELLIPSE TO A PROJECTED ORBIT

In a Cartesian coordinate system with +x-axis (East), +y-axis (North), +z-axis (pointing away from the Earth), and the origin

at the dynamical center, the coordinates giving the locus of an elliptical orbit projected on the plane of the sky must satisfy

$$\frac{(yT_{11} - xT_{21})^2}{(b\cos i)^2} + \frac{(xT_{22} + ae\cos i - yT_{12})^2}{(a\cos i)^2} = 1, \quad \text{(A1)}$$

where T_{ij} are the elements of the coordinate transformation matrix that is used to project the orbit plane onto the sky plane. T_{ij} are functions of the orbital angles (Ω, ω, i), that is,

$$T_{11} = +\cos\omega\cos\Omega - \sin\omega\sin\Omega\cos i$$

$$T_{12} = -\sin\omega\cos\Omega - \cos\omega\sin\Omega\cos i$$

$$T_{21} = +\cos\omega\sin\Omega + \sin\omega\cos\Omega\cos i$$

$$T_{22} = +\sin\omega\sin\Omega + \cos\omega\cos\Omega\cos i.$$

The other parameters required to describe the orbit geometry are the eccentricity e, semimajor axis a, and semiminor axis $b = a\sqrt{1-e^2}$. Using Equation (A1) as the input constraint equation for fitting an orbit, we utilized the LSQ subroutine LSQGEN of Brandt (1999), which is based on an algorithm of orthogonal transforms. The values of the orbital parameters are derived by this program along with their 1σ errors computed from the square root of the covariance matrix under the assumption that the measurement errors are small. The assumption of small measurement errors in the determination of the loci ($\sim\pm1\farcs25$, the radius of the circles in Figure 5(a)) is valid in this paper.

APPENDIX B

DYNAMICAL MASS CONSTRAINED BY RADIAL VELOCITIES

Under the assumption of Keplerian motion, the dynamical mass of a system can be constrained by the observed radial velocities at the projected location (x, y) and the five orbital parameters (a, e, Ω, ω, i) determined from the LSQ fit of the orbit geometry as discussed above,

$$V_z = \frac{M_{\rm dyn}^{1/2}}{\sqrt{a(1-e^2)}}\left[T_{32}\left(e + \cos\nu\right) - T_{31}\sin\nu\right], \quad \text{(B1)}$$

where ν is the angle of the true anomaly:

$$\cos\nu = \frac{a(1-e^2)}{er} - \frac{1}{e},$$

where r is the distance of the object with respect to the dynamical center:

$$r = \sqrt{(x\cos\Omega + y\sin\Omega)^2 + \frac{1}{\cos^2 i}(y\cos\Omega - x\sin\Omega)^2}, \quad \text{(B2)}$$

and the corresponding elements of the transformation matrix are

$$T_{31} = \sin\omega\sin i,$$
$$T_{32} = \cos\omega\sin i.$$

REFERENCES

Aitken, D. K., Gezari, D., Smith, C. H., McCaughrean, M., & Roche, P. F. 1991, ApJ, 380, 419
Aitken, D. K., Smith, C. H., Moore, T. J. T., & Roche, P. F. 1998, MNRAS, 299, 743
An, T., Goss, W. M., Zhao, J.-H., Hong, X. Y., Roy, S., Rao, A. P., & Shen, Z.-Q. 2005, ApJ, 634, L49
Becklin, E. E., & Neugebauer, G. 1975, ApJ, 200, L71
Blum, R. D., Sellgren, K., & Depoy, D. L. 1996, ApJ, 470, 864
Boulet, D. L. 1991, Methods of Orbit Determination (Virginia: Willmann-Bell, Inc.)
Bower, G. C., Roberts, D. A., Yusef-Zadeh, F., Backer, D. C., Cotton, W. D., Goss, W. M., Lang, C. C., & Lithwick, Y. 2005, ApJ, 633, 218
Brandt, S. 1999, Data Analysis: Statistical and Computational Methods for Scientists and Engineers (New York: Springer)
Chandrasekhar, S., & Fermi, E. 1953, ApJ, 118, 113
Doeleman, S. S., et al. 2008, Nature, 455, 78
Ekers, R. D., van Gorkom, J. H., Schwarz, U. J., & Goss, W. M. 1983, A&A, 122, 143
Geballe, T. R., Wade, R., Krisciunas, K., Gatley, I., & Bird, M. C. 1987, ApJ, 320, 570
Geballe, T. R., Najarro, F., Rigaut, F., & Roy, J.-R. 2006, ApJ, 652, 370
Geballe, T. R., Rigaut, F., Roy, J.-R., & Draine, B. T. 2004, ApJ, 602, 770
Genzel, R., Pichon, C., Eckart, A., Gerhard, O. E., & Ott, T. 2000, MNRAS, 317, 348
Ghez, A. M., et al. 2003, ApJ, 586, L127
Ghez, A. M., et al. 2005, ApJ, 620, 744
Ghez, A. M., et al. 2008, ApJ, 689, 1044
Gillessen, S., Eisenhauer, F., Trippe, S., Alexander, T., Genzel, R., Martins, F., & Ott, T. 2009, ApJ, 692, 1075
Glasse, A. C. H., Aitken, D. K., & Roche, P. F. 2003, Astron. Nachr., 324, 563
Herbst, T. M., Beckwith, S. V. W., Forrest, W. J., & Pipher, J. L. 1993, AJ, 105, 956
Krabbe, A., Genzel, R., Drapatz, S., & Rotaciuc, V. 1991, ApJ, 382, L19
Lacy, J. H., Achtermann, J. M., & Serabyn, E. 1991, ApJ, 380, L71
Lacy, J. H., Townes, C. H., Geballe, T. R., & Hollenbach, D. J. 1980, ApJ, 241, L132
Lebofsky, M. J., Rieke, G. H., & Tokunaga, A. T. 1982, ApJ, 263, 736
Liszt, H. S. 2003, A&A, 408, 1009
Lo, K. Y., & Claussen, M. J. 1983, Nature, 306, 647
Menten, K. M., Reid, M. J., Eckart, A., & Genzel, R. 1997, ApJ, 475, 111
Morris, M., & Yusef-Zadeh, F. 1987, in The Galactic Center, ed. D. C. Backer (Melville, NY: AIP), 127
Muno, M. P., Pfahl, E., Baganoff, F. K., Brandt, W. N., Ghez, A., Lu, J., & Morris, M. R. 2005, ApJ, 622, L113
Mužić, K., Kckart, A., Schödel, R., Meyer, L., & Zensus, A. 2007, A&A, 469, 993
Mužić, K., Schödel, R., Eckart, A., Meyer, L., & Zensus, A. 2008, A&A, 482, 173
Panagia, N. 1973, ApJ, 78, 929
Paumard, T., Maillard, J. P., & Morris, M. 2004, A&A, 426, 81
Paumard, T., Maillard, J. P., Morris, M., & Rigaut, F. 2001, A&A, 366, 466
Paumard, T., et al. 2006, ApJ, 643, 1011
Perger, M., Moultaka, J., Eckart, A., Viehmann, T., Schödel, R., & Mužić, K. 2008, A&A, 478, 127
Porquet, D., Grosso, N., Belanger, G., Goldwurm, A., Yusef-Zadeh, F., Warwick, R. S., & Predehl, P. 2005, A&A, 443, 571
Reid, M. J., Menten, K. M., Genzel, R., Ott, T., Schödel, R., & Eckart, A. 2003, ApJ, 587, 203
Reid, M. J., Menten, K. M., Trippe, S., Ott, T., & Genzel, R. 2007, ApJ, 659, 378
Roberts, D. A., & Goss, W. M. 1993, ApJS, 86, 133
Roberts, D. A., Yusef-Zadeh, F., & Goss, W. M. 1996, ApJ, 459, 627
Schödel, R., et al. 2002, Nature, 419, 694
Schwarz, U. J., Bregman, J. D., & van Gorkom, J. H. 1989, A&A, 215, 33
Serabyn, E., & Lacy, J. H. 1985, ApJ, 293, 445
Serabyn, E., Lacy, J. H., & Achtermann, J. M. 1991, ApJ, 378, 557
Serabyn, E., Lacy, J. H., Townes, C. H., & Bharat, R. 1988, ApJ, 326, 171
Tanner, A., Ghez, A. M., Morris, M., Becklin, E. E., Cotera, A., Ressler, M., Werner, M., & Wizinowich, P. 2002, ApJ, 575, 860
Tanner, A., Ghez, A. M., Morris, M. R., & Christou, J. C. 2005, ApJ, 620, 744
Viehmann, T., Eckart, A., Schödel, R., Pott, J.-U., & Moultaka, J. 2005, ApJ, 642, 861

Vollmer, B., & Duschl, W. J. 2000, New Astron., 4, 581
Wardle, M., & Yusef-Zadeh, F. 1992, Nature, 357, 308
Wollman, E. R., Smith, H. A., & Larson, H. P. 1982, ApJ, 258, 506
Yusef-Zadeh, F., & Melia, F. 1992, ApJ, 385, 41
Yusef-Zadeh, F., & Morris, M. 1991, ApJ, 371, L59
Yuzef-Zadeh, F., Morris, M., & Ekers, R. 1989, in IAU Symp. 136, The Center of The Galaxy, ed. M. Morris (Norwell, MA: Kluwer), 443
Yusef-Zadeh, F., Morris, M., & Ekers, R. D. 1990, Nature, 348, 45
Yusef-Zadeh, F., Roberts, D. A., & Biretta, J. 1998, ApJ, 503, L191
Yusef-Zadeh, F., & Wardle, M. 1993, ApJ, 405, 584
Zhao, J.-H., & Goss, W. M 1998, ApJ, 499, L163
Zhao, J.-H., & Goss, W. M 1999, in ASP Conf. Ser. 186, The Central Parsecs of the Galaxy, ed. H. Falcke, A. Cotera, W. J. Duschl, F. Melia, & M. J. Rieke (San Francisco, CA: ASP), 224
Zhao, J.-H., Goss, W. M., Lo, K. Y., & Ekers, R. D. 1991, Nature, 354, 46